Supplementary Information

Navigating Low State of Charge Phase Transitions in Layered Cathodes for Long-Life Sodium-Ion Batteries

Wenda Li,‡[a] Zhaoyue Li, ‡[b] Lizhi Li,‡ [a] Alice J. Merryweather,[cd] Yilin Chen,[e] Shaoyu Yang,[a] Hao Shi,[f] Yang Lu,[a] Yixiao Qiu,[a] Guangsu Tan,[a] Zhipeng Chen,[a] Weiwei Wang,[g] Yuzhu Wang,[g] Yi-Fan Huang,[a] Zhengyan Lun,[fh] Christoph Schnedermann,[d] Xiangwen Gao,*[i] Jingyang Wang,*[b] Clare P. Grey,*[c] Chao Xu*[a]

[a] School of Physical Science and Technology, ShanghaiTech University, Shanghai, China.

[b] School of Sustainable Energy and Resources, Nanjing University, Suzhou, China.

[c] Yusuf Hamied Department of Chemistry, University of Cambridge, Cambridge, UK.

[d] Illumion Ltd., Cambridge, UK.

[e] In-Situ Center for Physical Sciences, School of Chemistry and Chemical Engineering, Shanghai Jiao Tong University, Shanghai, China.

[f] Binzhou Institute of Technology, Weiqiao-UCAS Science and Technology Park, Binzhou, Shandong Province, China.

[g] Shanghai Synchrotron Radiation Facility, Shanghai Advanced Research Institute, Chinese Academy of Sciences, Shanghai, China.

[h] School of Chemical Sciences, University of Chinese Academy of Sciences, Beijing, China.

[i] Future Battery Research Center, Global Institute of Future Technology, Shanghai Jiao Tong University, Shanghai, China.

‡ These authors contributed equally to this work

Corresponding authors:

Chao Xu: xuchao1@shanghaitech.edu.cn

Clare P. Grey: cpg27@cam.ac.uk

Jingyang Wang: jy_wang@nju.edu.cn

Xiangwen Gao: xiangwen.gao@sjtu.edu.cn

Experimental section

Materials synthesis

Polycrystalline NFM materials. $NaNi_{1/3}Fe_{1/3}Mn_{1/3}O_2$, $Na_{0.96}Ca_{0.02}Ni_{1/3}Fe_{1/3}Mn_{1/3}O_2$ and $Na_{0.92}Ca_{0.04}Ni_{1/3}Fe_{1/3}Mn_{1/3}O_2$ (denoted as NFM, NFM-Ca2 and NFM-Ca4, respectively) were synthesised via a solid-state reaction method using $Ni_{1/3}Fe_{1/3}Mn_{1/3}(OH)_2$ (Jinghe New City Shaanxi Coal Technology Research Institute New Energy Materials Co., Ltd), Na_2CO_3 (Aladdin, ≥ 99.8 %) and $CaCO_3$ (Aladdin, ≥ 99.99 %) as precursors. Stoichiometric amounts of Na_2CO_3, $CaCO_3$ and $Ni_{1/3}Fe_{1/3}Mn_{1/3}(OH)_2$ were mixed and ground with ethanol for 20 minutes to ensure uniform mixing, followed by drying at 60 °C for 10 min. The mixed precursor was calcined in air at 850 °C for 15 hours with a heating and cooling rate of 5 °C min^{-1}. Upon cooling to 150 °C, the sample was immediately transferred to an argon (Ar) -filled glovebox (O_2 < 1 ppm, H_2O < 1 ppm).

Single-crystal NFM materials. Single-Crystal $NaNi_{1/3}Fe_{1/3}Mn_{1/3}O_2$ was synthesised via a solid-state reaction method. Stoichiometric amounts of Na_2CO_3 (5.0 % excess, molar ratio 1:1.05, Aladdin, ≥ 99.8 %), $NiCO_3 \cdot 2Ni(OH)_2 \cdot xH_2O$ (x≈1.8 for lot#J2218099; Aladdin, ≥ 99.99 %), MnO_2 (Aladdin, ≥ 99 %) and Fe_2O_3 (Aladdin, ≥ 99.9 %) were mixed and ball-milled at 250 rpm for 8 h. The resulting mixture was pelletised and calcined in air with a heating rate of 5 °C min^{-1} to 1050 °C, held for 1 h, then cooled at 2 °C min^{-1} to 950 °C and calcined for an additional 15 h. Upon further cooling at 2 °C min^{-1} to 150 °C, the sample was promptly transferred to an Ar-filled glovebox.

Electrochemical characterisations

Electrode preparation. The NFM cathode electrodes were fabricated using a nitrogen (N_2) -protected wet coating method.[1] A mixture of 90 wt% active materials, 5.0 wt% Super P (Timcal) and 5.0 wt% polyvinylidene fluoride (PVDF, HSV 900, Arkema, prepared as a 4.0 wt% PVDF solution in 96 wt% N-methyl-2-pyrrolidone (NMP, J&K Scientific)) was weighed and mixed in the Ar-filled glovebox. The prepared slurry was coated onto Al foil inside a N_2-filled glovebox (relative humidity, RH = 5.0–15 %) and dried at 80 °C for 30 min under N_2 protection. After drying, the electrodes were calendared to the desired thickness, cut into an effective area of 25 mm × 25 mm squares, and welded with Al tabs. The mass loading of active materials on the cathode electrode is about 7.1~7.3 mg cm^{-2}. The areal loading was intentionally set to a relatively low value to avoid sodium plating on the anode, which significantly impacts the ageing mechanism of full cells. The hard carbon electrodes were prepared in air. A mixture containing 95 wt% hard carbon (HC, Kuraray, Type 2), 1.0 wt%

Super P, 2.0 wt% carboxymethylcellulose sodium (CMC, Nippon Paper Industries Co., Ltd., prepared as a 1.5 wt% CMC solution in 98.5 wt% pure water) and 2.0 wt% styrene-butadiene rubber (SBR, Shenzhen kejing star technology Co., Ltd.) was weighed and mixed. The slurry was coated onto Al foil and dried at 100 °C for 40 min. After drying, the electrodes were calendared, cut into 26 mm × 26 mm, and welded with Al tabs. The mass loading of active materials on the anode electrode is about 3.8~4.0 mg cm^{-2}. For full cells with Ca-doped materials, the anode was prepared using a composition of 95 wt% HC and 5.0 wt% sodium alginate (SA, Sigma-Aldrich). The slurry preparation and coating processes were the same as the CMC/SBR method. All electrodes were vacuum-dried at 120 °C for 12 h in the vacuum oven. After drying, the samples were allowed to cool to room temperature and were immediately transferred to an Ar-filled glovebox.

Battery assembly. In this study, all pouch cells were single-layer full cells. The cathode was a 25 mm × 25 mm electrode coated with active materials, while the anode was a 26 mm × 26 mm HC electrode, and the N/P ratio was approximately 1.12. Celgard 2500 was used as the separator, and the electrolyte consisted of 1 M $NaClO_4$ in ethylene carbonate (EC): ethyl methyl carbonate (EMC) (3:7 by volume) with 5.0 vol% fluoroethylene carbonate (FEC, Jiangsu HSC New Energy Materials Co., Ltd) and 1.0 wt% propene sulfone (PES, Adamas, ≥ 99.93 %) as additives. Assembly was conducted in an Ar-filled glovebox, where the cathode, separator, and anode were carefully aligned and thermally sealed on three sides. Finally, 200 μL of electrolyte was added, and the pouch cell was vacuum-sealed. Coin cells (2032-type, 316L, Canrd) were used to perform a preliminary electrochemical performance evaluation of the synthesised materials. The cathode was prepared as a 12 mm-diameter circular electrode coated with active material, while the anode consisted of a 16 mm-diameter metallic sodium disc (99.8%, Sigma-Aldrich). A glass fiber (GF/B, Whatman) was used as the separator. The electrolyte consisted of 1 M $NaClO_4$ dissolved in a mixed solvent of EC and EMC with a volume ratio 3:7, supplemented with 5.0 vol% FEC. The coin cells were assembled in an Ar-filled glove box.

Electrochemistry. The electrochemical performance of the batteries was tested using a LAND battery testing system (LANHE CT3002A, Wuhan LAND Electronics Co., Ltd.). For half cells, a constant current charge-discharge mode was employed within a voltage window of 2.0 V–4.0 V (vs. Na/Na^+). The cells were first cycled at a 0.1C rate (14.5 mA g^{-1}) for two cycles, followed by long-term cycling at a 1C rate (145 mA g^{-1}). During rate capability testing, the cells were cycled five times at each rate of 0.1C, 1C, 4C (580 mA g^{-1}), 8C (1160 mA g^{-1}), and again at

0.1C within the same charge-discharge voltage window. For full cells, a constant current-constant voltage (CC-CV) charging and a constant current (CC) discharging mode were used. All full cells were initially cycled at a 0.05C rate (7.25 mA g^{-1}) for two formation cycles within a voltage window of 0.5 V–3.8 V or 0.5 V–3.9 V, followed by aging cycles at a 1C rate (145 mA g^{-1}). If the discharge cut-off voltage was adjusted during subsequent testing, the cells were first cycled at a 0.05C rate for two cycles within the updated voltage window (e.g., 1.5 V or 2.0 V–3.8 V) before continuing 1C rate cycling. The 3C (435 mA g^{-1}) rate cycling was conducted within a voltage window of 0.5–3.8 V. Electrochemical impedance spectroscopy (EIS) was performed using an electrochemical workstation (Solartron Analytical, 1470E; Gamry, Interface 1010E) over a frequency range of 100 kHz to 10 mHz with an amplitude of 10 mV. The EIS data were analysed and fitted using Zview4 software. All battery tests were conducted in a temperature-controlled chamber (LBI-300HT, Shanghai Longyue Instrument Equipment Co., Ltd.) maintained at 25 ± 1 °C.

Materials characterisations

Powder X-ray diffraction (PXRD). The laboratory XRD data were collected using a Bruker D8 Advance diffractometer with Cu Kα radiation (wavelength λ = 1.5406 Å). The measurement was performed with a step size of 0.02° and an exposure time of 1 s per step. Synchrotron powder diffraction data were collected at beamline 17UM (BL17UM) of the Shanghai Synchrotron Radiation Facility (SSRF) using a wavelength of 0.4834 Å. Two-dimensional diffraction patterns were acquired with an EIGER2 X-16M detector and subsequently converted to one-dimensional data using Dawn software[2].

***Operando* XRD.** The *operando* XRD data were also collected at the SSRF-BL17UM beamline with a wavelength of 0.6209 Å, using the same data collection method as ex situ PXRD, with an exposure time of 20 s for each pattern. The pouch cell used in the tests was preconditioned by cycling twice at a 0.05C rate within a voltage window of 0.5 V to 3.8 V, followed by 10 cycles at a 1C rate within the same voltage window. The electrochemical window for *operando* testing was 0.5 V to 3.8 V, with CCCV charging to control the total charging time to 1 h, and discharging was performed under constant current mode. The PXRD and *operando* XRD data were subjected to Rietveld refinement using the TOPAS software (version 5).

***Operando* Charge Photometry**. Particle cracking and (de)sodiation were observed at the individual particle level and under *operando* conditions using the illumionONE charge photometer – an optical scattering microscopy technique – developed by Illumion Ltd. An

optically-accessible coin cell (CP coin cell, Illumion Ltd.) was assembled with a sodium metal counter electrode, glass microfibre separator (Whatman GF/B), and a free-standing NFM working electrode, such that the working electrode could be imaged. The free-standing electrode consisted of 60 % active materials, 20 % polytetrafluoroethylene (PTFE) binder and 20 % carbon black, and the typical mass loading for the active material was 5 mg cm^{-2}. The cell contained 150 µL of electrolyte, consisting of 1M $NaPF_6$ (Acros Organics) dissolved in 93% propylene carbonate (PC) and 7% fluoroethylene carbonate (FEC). The cell was cycled in a voltage range of 2.0 V to 4.0 V (vs. Na/Na^+) for 6 cycles (including CC-CV protocols at C/10 and C/3 rates) prior to performing the cycle presented in Fig. 3b. For the presented cycle, the cell was (dis)charged with a CC-CV protocol, with a 1C rate (130 mA g^{-1}), a 1-hour voltage hold following by a 1-hour OCV period at the top of charge, and a 4-hour voltage hold at the bottom of charge. Images were recorded every 10 s (during the constant-current steps) or 20 s (otherwise).

Electron microscopy. The morphology and elemental distribution of the pristine NFM material and the doped materials were characterised using scanning electron microscopes (SEM, Regulus8100, Hitachi High-Technologies Co., Ltd and TESCAN MIRA3) coupled with an energy-dispersive X-ray spectrometer (EDS, EDAX). The pristine and cyclically aged polycrystalline materials were cross-section polished for 3 h at 3 kV using an Ar ion beam milling instrument (Model 1061 SEM mill, Fischione). After polishing, the samples were vacuum-transferred to the SEM (Regulus8240, Hitachi High-Technologies Co., Ltd) for morphological characterisation.

X-ray absorption spectroscopy (XAS). The synchrotron-based XAS data were collected at the SSRF BL16U1 beamline, using a Si(111) double crystal monochromator, under vacuum in transmission mode. The K-edge absorption spectra of Ni, Fe, and Mn foils were measured for energy calibration (i.e., Ni K-edge = 8333 eV, Fe K-edge = 7112 eV, and Mn K-edge = 6539 eV). The energy calibration of the Ca K-edge was carried out using calcite as the standard reference, by aligning the peak maximum of its first-order derivative spectrum to 4046.06 eV.[3] The acquired XAS spectra were processed using the ATHENA software package, including energy calibration, deglitching, and normalization.[4] The extended X-ray absorption fine structure (EXAFS) signal, $\chi(k)$, was k^3-weighted to enhance high-energy oscillations, and Fourier transforms were performed in the 2.5–10.0 $Å^{-1}$, 3.0–10.0 $Å^{-1}$, and 2.5–9.5 $Å^{-1}$ ranges for the Ni, Fe, and Mn K-edges, respectively, and in the 3.0–8.0 $Å^{-1}$ range for the Ca K-edge.

Nonlinear least-squares fitting of the data was carried out using the amplitude and phase functions generated by the FEFF6 code to extract the EXAFS structural parameters.

X-ray photoelectron spectroscopy (XPS). The electrodes were characterised using an ESCALAB 250Xi instrument (Thermo Fisher SCIENTIFIC) equipped with an Al Kα X-ray source (hν = 1486.7 eV). After cycling, the pouch cell was directly disassembled at the fully discharged state. The electrode sheets were rinsed with dimethyl carbonate (DMC) for 10 min, then dried at room temperature under vacuum for 30 min. The samples were then transferred to the XPS chamber under vacuum for analysis. All spectra were calibrated using the C–C peak at 284.8 eV, and the spectra were fitted using Avantage software.

Inductively coupled plasma-optical emission spectroscopy (ICP-OES). The chemical composition of the initial materials was analysed using Inductively Coupled Plasma Optical Emission Spectroscopy (ICP-OES, iCAP 7400).

Mössbauer spectroscopy. The ^{57}Fe Mössbauer spectra were collected using a Mössbauer spectrometer equipped with a Topologic 500A spectrometer detector and a ^{57}Co (Rh) radiation source. The velocity was calibrated by a standard α-Fe foil.

Raman Spectroscope. The electrode samples were fabricated via a dry-process method by homogeneously blending the active material, conductive carbon black, and PTFE at a mass ratio of 8:1:1, followed by calendaring into freestanding electrodes. Sodium metal half-cells were assembled using an electrolyte of 1 M $NaClO_4$ in EC/EMC (3:7 v/v) with 5 vol% FEC, along with a bilayer separator system (GF/B glass fibre and Celgard 2500 microporous membrane) to mitigate cathode-electrolyte interfacial contamination. After electrochemical cycling within 2.0–4.0 V (vs. Na/Na^+) at 0.1C (14.5 mA g^{-1}), the cells were disassembled in the Ar-filled glovebox, and the electrodes were washed with DMC to remove residual electrolytes, then immobilised on a quartz glass substrate using Kapton tape to prevent air exposure. Ex situ Raman spectroscopy was performed using a Renishaw inVia confocal Raman microscope system (532 nm laser excitation) with a spectral acquisition time of 40 s per scan. The quartz substrate minimised fluorescence background interference, preserving the sample's intrinsic chemical state.

Differential Electrochemical Mass Spectrometry (DEMS). The in situ gas analysis was performed using a custom-built battery coupled with a HIDEN HPR-20 EGA differential electrochemical mass spectrometer. The electrolyte consisted of 1 M $NaPF_6$ in EC/PC (1:1 v/v). The cathode was prepared using the same dry-process method as those for Raman testing.

High-purity helium (He) served as the carrier gas to continuously transfer the generated gases to the mass spectrometer for real-time analysis of gas-phase products based on their mass-to-charge ratios (m/z).

Computational methods

Density Functional Theory (DFT) calculations

All DFT calculations in this study were carried out using the Vienna ab initio Simulation Package (VASP) code. The exchange–correlation effect was described via the generalised gradient approximation (GGA) with the form of Perdew–Burke–Ernzerhof (PBE). A Hubbard U potential correction[5] was applied to account for the electronic correlation effects of transition-metal 3*d* electrons in Ni (6.2 eV), Fe (5.3 eV) and Mn (3.9 eV) ions.[6] The DFT calculations employed an energy cutoff of 520 eV,[7, 8] and added the DFT-D3 method with zero-damping function correction. Ions were fully relaxed in the optimisation with the energy and force convergence criterion of 10^{-5} eV and 0.01 eV $Å^{-1}$, respectively.

Bulk phase model of O3-NFM and O3-NFM-Ca systems. Two types of atomic ordering are considered, i.e., transition metal (TM) ordering and Na/Ca ordering. Both these orderings are enumerated in a 3 × 3 × 1 supercell and calculated by DFT, and the ones with the lowest energy were selected for further analysis. A 3×3×1 supercell of O3-$NaMnO_2$ with $R\bar{3}m$ symmetry was first constructed for the TM ordering. We then performed elemental substitution, and structures with various TM ordering were generated using an enumeration algorithm as part of the pymatgen code base. The generated structures were ranked by Ewald electrostatic energy ranking using the pymatgen library[6] and the top 20 structures were calculated using VASP, while the one with the lowest DFT energy was determined as the ground-state TM ordering. In the obtained ground-state TM ordering, Mn, Ni and Fe ions form a triangular lattice, respectively, therefore the highly-charged Mn^{4+} ions are uniformly separated (Figure S19).

Based on the ground-state TM ordering, the Na/Ca-vacancy orderings at various SOC were determined using a similar approach. The pymatgen library was used to enumerate various orderings and perform Ewald electrostatic energy ranking, among which the five lowest-energy structures were selected. VASP was then used to determine each SOC's most stable Na/Ca-vacancy orderings. The relevant structure is shown in Figure S19.

The density of states (DOS), band structure, and Bader charge were calculated for $Na_{1-x}Ni_{1/3}Fe_{1/3}Mn_{1/3}O_2$ (NFM) and $Na_{25/27-x}Ca_{1/27}Ni_{1/3}Fe_{1/3}Mn_{1/3}O_2$ (NFM-Ca) at various SOCs,

i.e., x=4/27, 6/27, 8/27, 10/27, to investigate the atomic and electronic variation upon charging.

Bulk phase model of P3-NFM and P3-NFM-Ca systems. For the structure of the P3 phase, we constructed 3×3×1 P3-$NaCoO_2$ supercells with R3m symmetry and the transition metal layer using the TM ordering determined in the O3 phase. Then we used a similar approach to determine the Na/Ca vacancy ordering of the P3 phase near the phase transition point. That is, the pymatgen library was used to enumerate the various orderings and the Ewald electrostatic energy ordering, from which the five structures with the lowest energies were selected, and the most stable Na/Ca vacancy ordering was determined using VASP.

Numerical Simulations

Numerical modelling was used to simulate the stress evolution in the NFM and calcium-substituted NFM (NFM-Ca4), particularly during the low SOC region of discharge at a 1C rate, which matches the experimental conditions. We assume a uniform sodium flux is applied to the particle's surface, with its magnitude determined from the C rate (i.e., 1C). The sodium diffusion in the NFM materials is governed by Fick's law $dc/dt = D\nabla^2 c$, where c is the sodium concentration in the cathode material, and D is the sodium diffusivity. The value used is $D_{a\text{-}b}$ = 1×10^{-10} cm^2/s,[9] and the diameter of the particle is set to 10 μm. The sodium insertion/extraction-induced strain fields are set according to the evolution of unit cell size, obtained by summing the P3 and O3 unit cells after correcting their phase fractions and the lattice parameters from the *operando* XRD results (Figure 4f). The stress field is analysed through the principles of elasticity theory, and Young's modulus and Poisson's ratio are 175 GPa and 0.3, respectively.[9] The governing equations are solved numerically using the electrochemical and mechanics modules in COMSOL Multiphysics software.

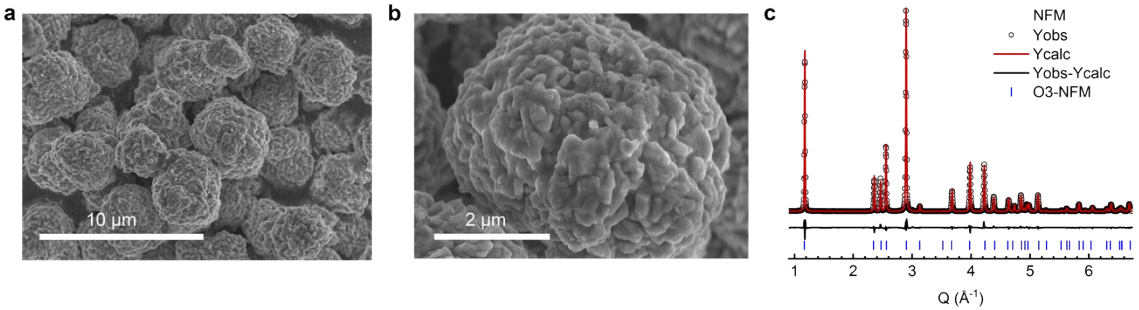

Figure S1. Pristine polycrystalline NFM. SEM image (a, b) and high-resolution synchrotron PXRD (c).

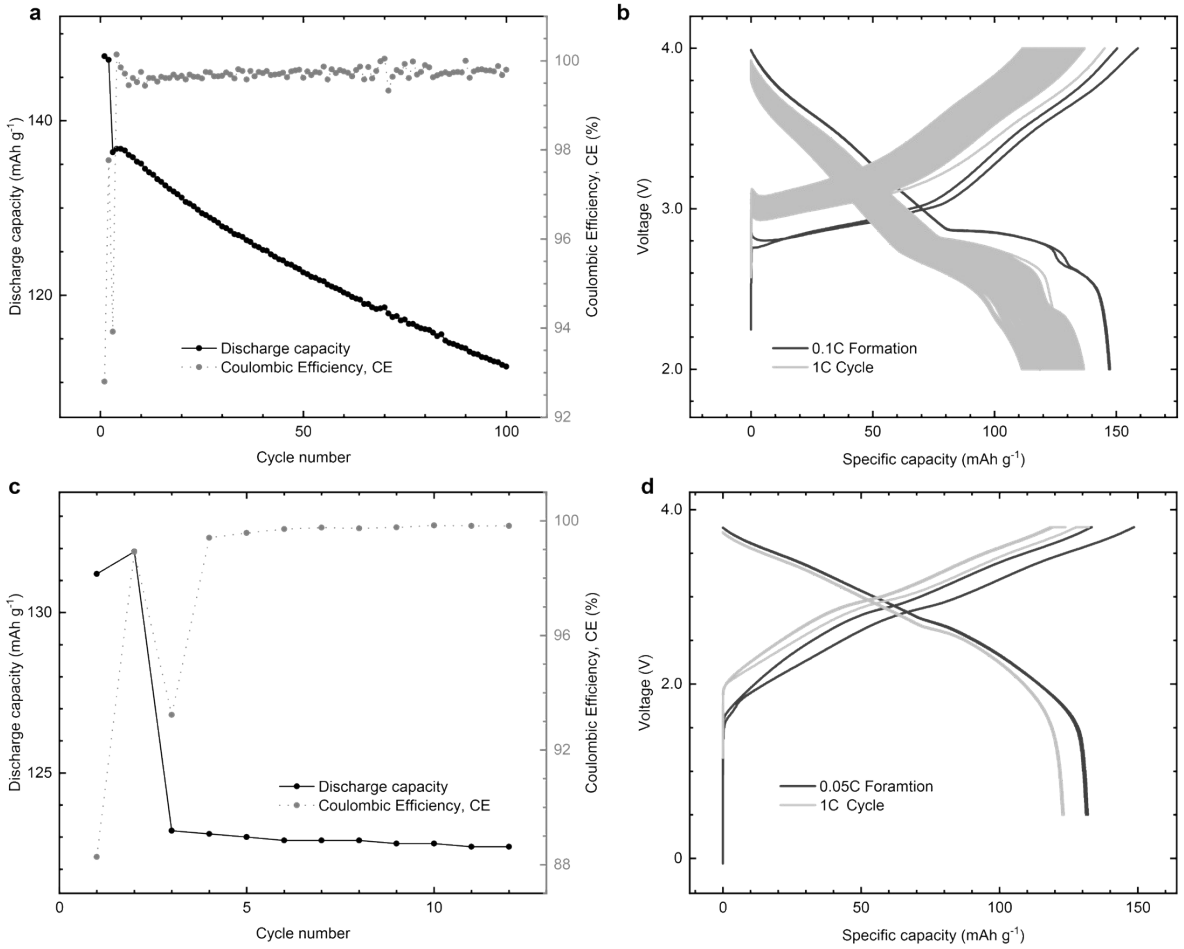

Figure S2. Electrochemical performance of NFM/Na half-cell and NFM/HC full cell. (a-b) Cycling performance of NFM/Na half-cell at 1C rate after two formation cycles at 0.1C rate (a) and voltage profiles (2.0 V – 4.0 V) during cycling (b). (c-d) Cycling performance of NFM/HC full cell at 1C rate after two formation cycles at 0.05C rate (c) and voltage profiles (0.5 V – 3.8 V) during cycling (d). The NFM/HC full cell was activated by cycling, with each cycle consisting of a constant current (CC) charge to 3.8 V, followed by constant voltage (CV) charging at 3.8 V, and then CC discharge to 0.5 V.

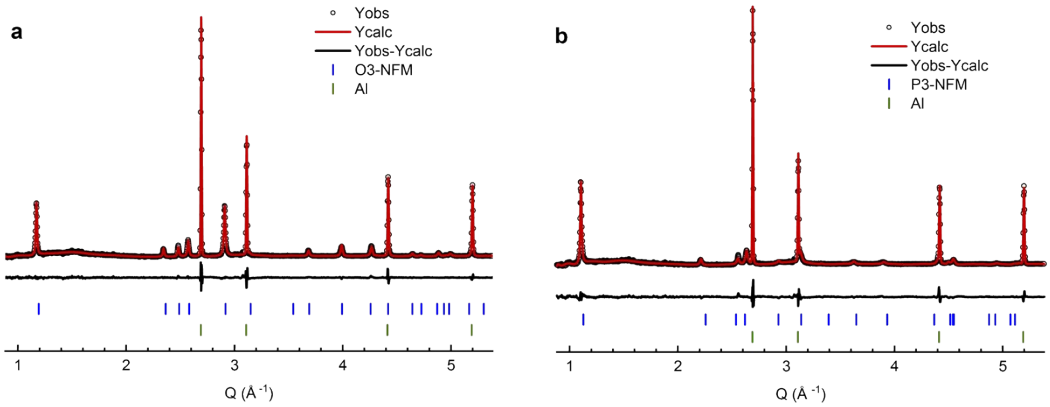

Figure S3. Operando PXRD of NFM/HC full cell. The first PXRD pattern at the start of charging (a) and the last PXRD pattern at the end of charging (b).

Supplementary Note 1: Estimation of Sodium (Na) Content

The estimation of the nominal sodium content in the NFM cathode of full cells during the 11th ageing cycle (during which the *operando* PXRD was taken)—following two formation cycles at a 0.05C rate and ten subsequent ageing cycles at a 1C rate— is based on electrochemical data. The difference between each cycle's charge and discharge capacities was calculated during the initial 0.05C formation process and the subsequent 1C cycling process, totalling 10 cycles. By summing these differences over 12 cycles, we attributed this capacity primarily to the Loss of Sodium Inventory (LSI), a result of solid electrolyte interphase (SEI) formation. This LSI corresponds to the deviation in sodium content in the cathode from its fully sodiated state. Using Rietveld refinement, the estimated sodium content derived from electrochemistry was further verified for the 0.5 V condition, which contains only the O3 phase. The value obtained, 0.86(1), aligns well with the electrochemical calculation of 0.866. This method enables us to correlate changes in the sodium content of the NFM cathode in full cells during discharge, as demonstrated in Figure S4.

To estimate the SOC range during which the P3-O3 transition occurs during discharge, we explored the Rietveld refinement for phase fraction analysis of the P3 and O3 phases. However, the large number of variables impacted the reliability of this method. We then employed two alternative approaches: examining the fractions of the (003) peak areas for both the O3 and P3 phases (Figure S4c) and analysing the integral of the (104) peak (Figure S4d). The first method is based on separating the (003) peak for the O3 and P3 phases, as shown in Figure 1, allowing for feasible peak fitting. The second method utilises the significantly lower intensity of the (104) peak for the P3 phase than the O3 phase, resulting in a noticeable increase when the O3 phase emerges (Figure 1). Both approaches yielded consistent results, showing that the O3 phase begins to appear at approximately $N_{a0.66}TMO_2$, where the (003) peak for the O3 phase becomes visible and the integral of the (104) peak increases significantly. The P3-O3 phase transition occurs rapidly initially, indicated by the sharp change in peak area fractions and the integral, but the P3 phase remains present until the end of discharge. This persistence is evidenced by the presence of the (003) peak of the P3 phase at 2.0 V and 1.5 V, as shown in Figures S4e,f.

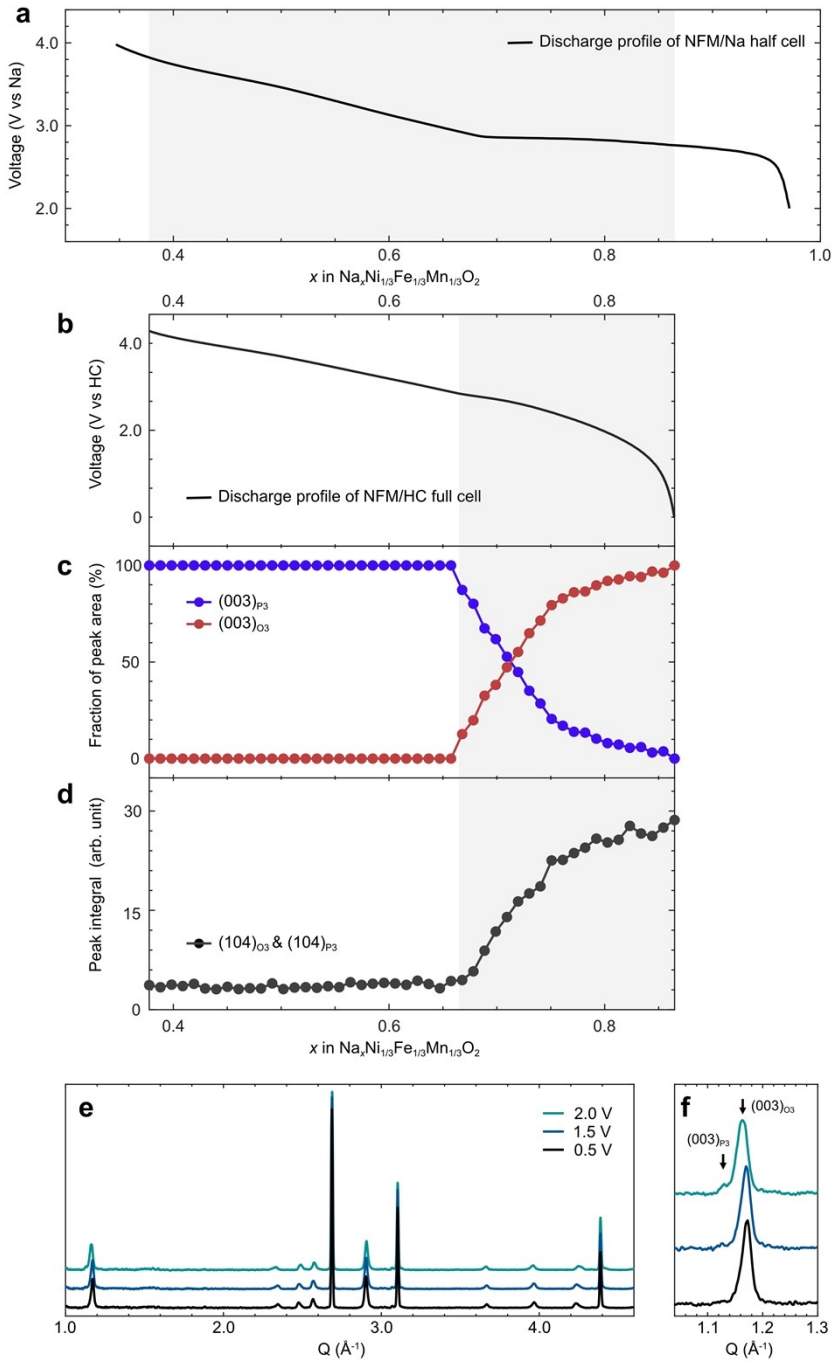

Figure S4. Discharge profiles and phase transition analysis of the NFM cathode in both half and full cells. (a) Voltage profile of NFM/Na half cell during discharge. The shaded regions in plot (a) indicate the SOC range during which the NFM is cycled in the full cell based on plot (b). (b) Voltage profile of NFM/HC full cell during discharge. (c) Evolution of the fraction of the (003) peak area attributed to P3 (blue) and O3 (red) phases during discharge. (d) The integral of the (104) peak for both O3 and P3 phases. (e) PXRD patterns at different voltages (2.0 V, 1.5 V, and 0.5 V). (f) Detailed view of the (003) peak for both P3 and O3 phases. The shaded regions in plots (b-d) indicate the SOC range during which the P3 and O3 phases coexist.

Supplementary Note 2: Raman spectroscopy results

The pristine NFM's Raman spectra exhibit characteristic peaks at 496.4 cm^{-1} and 579.7 cm^{-1}, which correspond to the E_g and A_{1g} vibrational modes, as illustrated in Figure S5. These results are in good agreement with the literature's typical Raman results for layered oxide cathode materials.[10] The A_{1g} mode specifically results from symmetrical oxygen stretches along the *c*-axis primarily. In contrast, the E_g mode entails oxygen atoms in adjacent parallel layers moving in opposite directions, as illustrated in Figure S5.

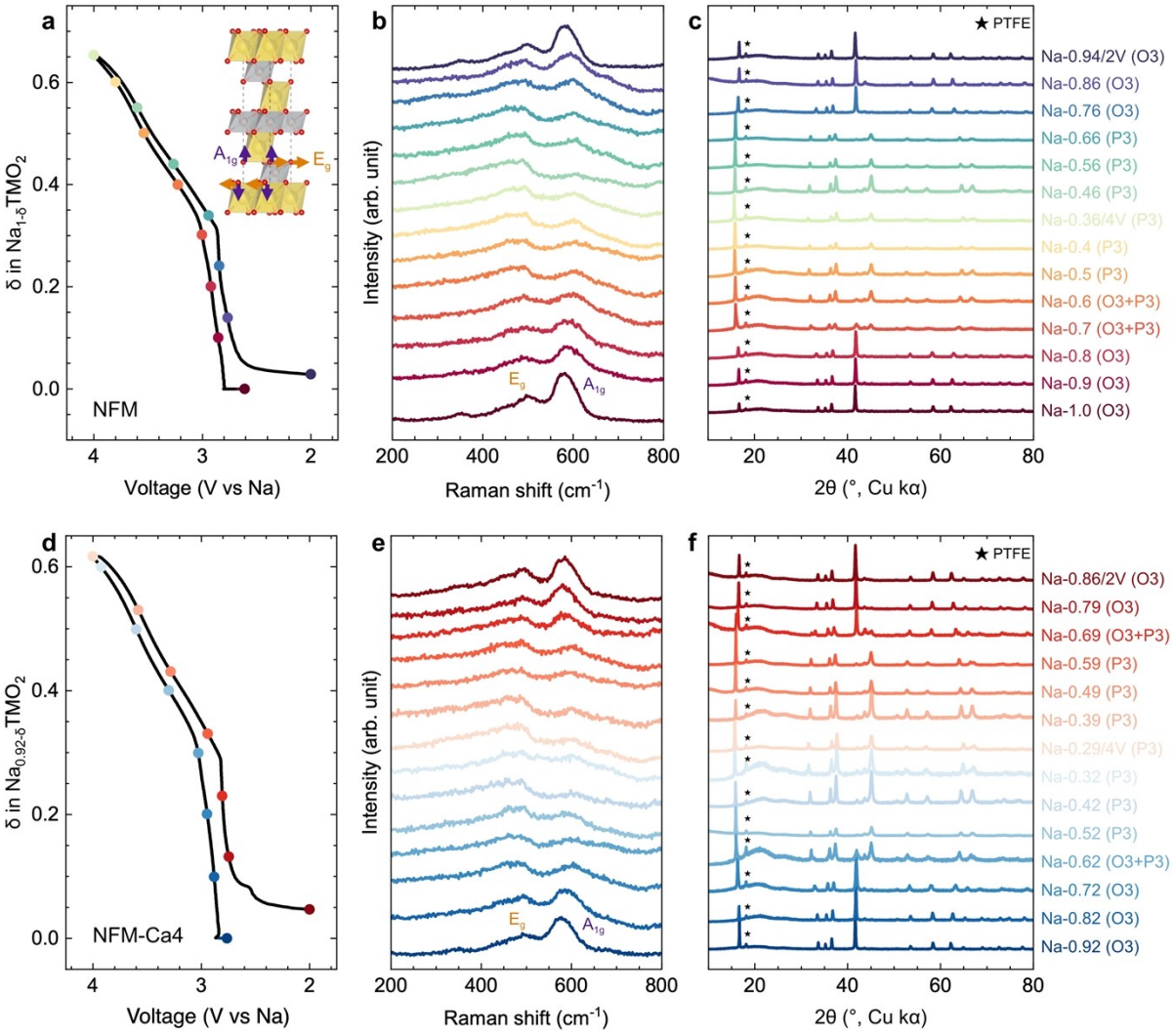

Figure S5. Raman spectroscopy results of NFM and NFM-Ca4 cathodes at various SOCs. (a-c) The voltage profile for the first cycle and structural illustrations for the A_{1g} and E_g Raman modes (a), Raman spectra (b) and the XRD patterns (c) of the NFM cathode at different SOCs. (d-f) The voltage profile for the first cycle (d), Raman spectra (e) and the XRD patterns (f) of the NFM-Ca4 cathode at different SOCs.

During Na extraction, the position and relative intensities of the E_g and A_{1g} peaks undergo alterations as the structure transitions from O3 to P3. Specifically, the E_g peak shifts to a lower wavenumber, while the A_{1g} peak moves to a higher wavenumber. Additionally, the intensity of the A_{1g} peak diminishes compared to the E_g as the structure changes from O3 to P3. Upon discharge, these trends reverse as sodium is reinserted into the structure, transitioning from P3 back to O3. The same phenomena are observed for the NFM-Ca4 cathode, as shown in Figure S5.

Table S1. Lattice parameters of the O3 phase at 2.0 V, 1.5 V and 0.5 V for fresh full cells.

Sample group：$R\bar{3}m$ α=β=90°，γ=120°				
Sample	a/Å	c/Å	vol/Å^3	Na-layer/ Å
2.0 V	2.9506(1)	16.2100(9)	122.219(6)	3.2561
1.5 V	2.9593(1)	16.1377(8)	122.390(5)	3.2315
0.5 V	2.9649(1)	16.0973(9)	122.545(3)	3.2173

Please note that the lattice parameters in this table differ slightly from the values provided in the main discussion (see Section: **Structural Change During Cycling of Full Cells at 1C Rate**). However, the general trend remains consistent across both datasets. This discrepancy arises because the results presented in Table S1 were derived from additional measurements conducted with significantly higher X-ray flux and longer exposure times. These adjustments were made to enhance the signal-to-noise ratio, thereby ensuring a more reliable refinement for the oxygen position, which was subsequently used to determine the Na layer slab size. Furthermore, these experiments were conducted on a different cell, which may also contribute to the minor discrepancies observed.

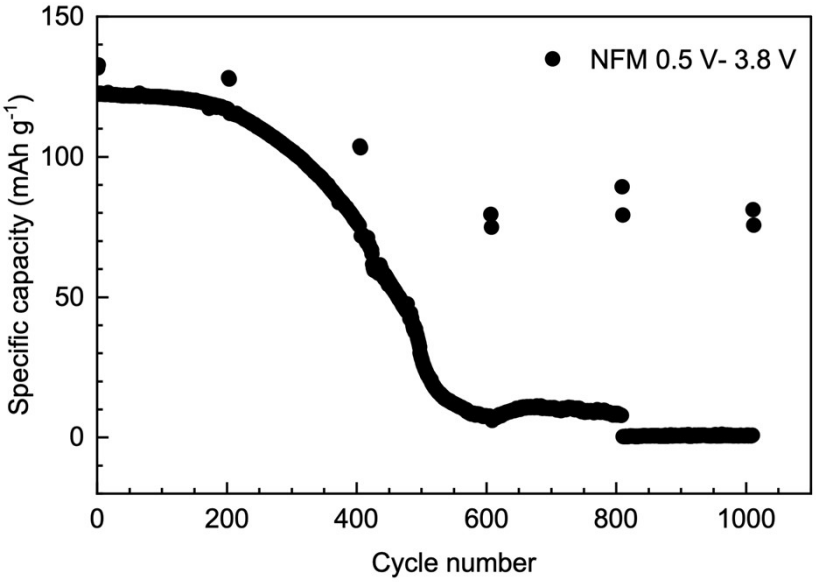

Figure S6. Full cycling history of the NFM/HC cell cycled with a voltage window of 0.5 – 3.8 V.

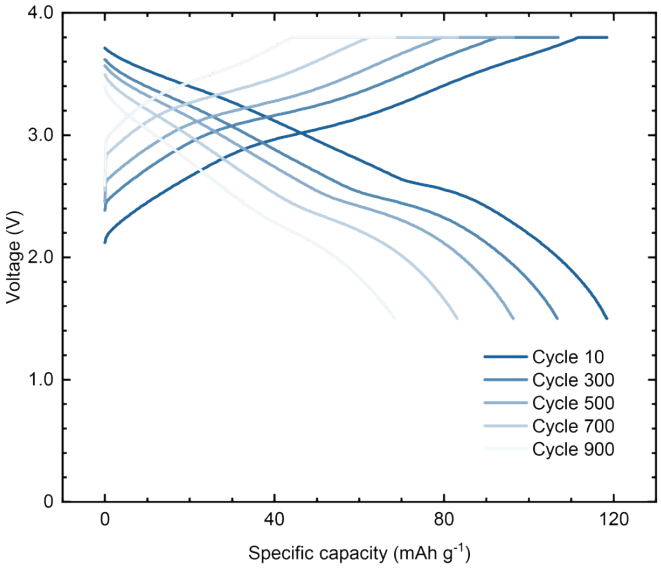

Figure S7. Voltage-capacity profiles for the 1.5 V LCV cell at cycles 10, 300, 500 and 900.

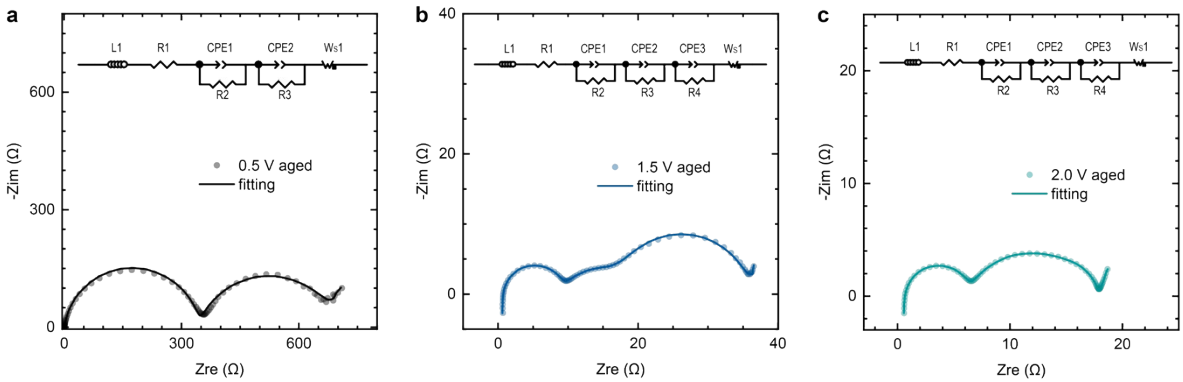

Figure S8. EIS fitting analysis of aged cells after 600 cycles under different LCV conditions. (a) 0.5 V aged. (b) 1.5 V aged. (c) 2.0 V aged. The total impedance is the sum of R1, R2, R3 and R4 (if relevant).

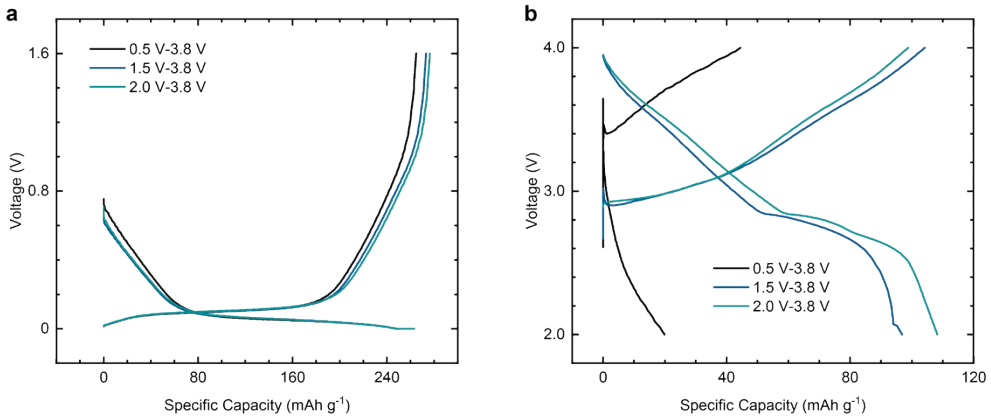

Figure S9. Electrochemical performance of refreshed NFM/Na and HC/Na cells. (a) Voltage-capacity profiles for the HC anodes extracted from the 0.5 V aged, 1.5 V aged, and 2.0 V aged full cells, reassembled into HC/Na half-cells and cycled between 1.6 V and 0.005 V. (b) Voltage-capacity profiles for the NFM cathodes extracted from the 0.5 V aged, 1.5 V aged and 2.0 V aged full cells, reassembled into NFM/Na half-cells and cycled between 2.0 V and 4.0 V.

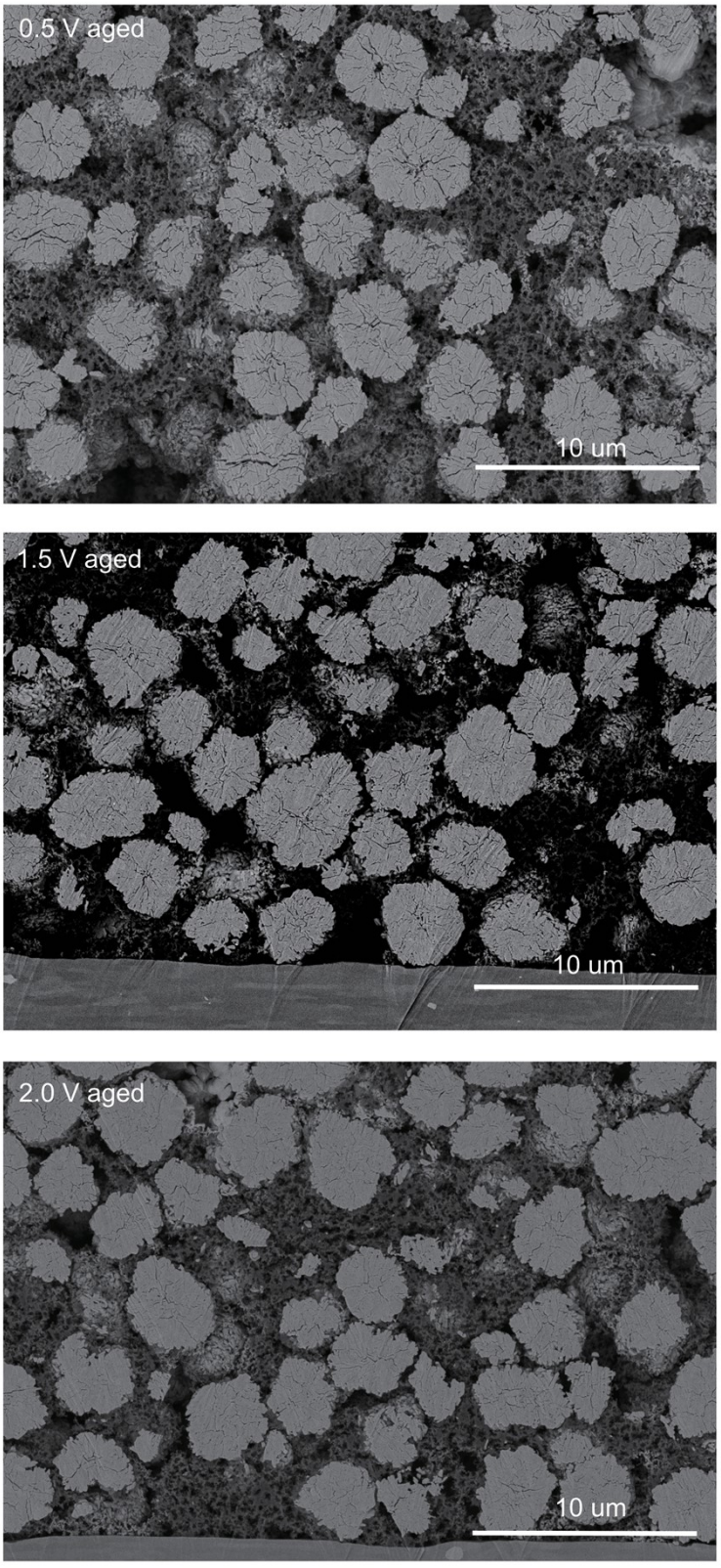

Figure S10. Cross-sectional SEM images of 0.5 V aged, 1.5 V aged, and 2.0 V aged cathode electrodes at low magnification.

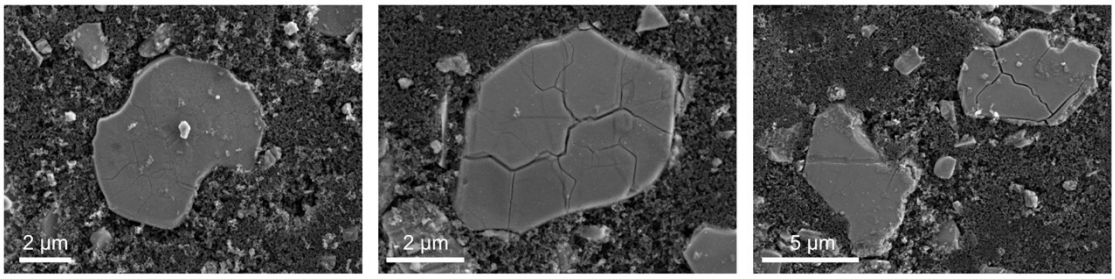

Figure S11. SEM images of cracked single-crystal NFM after cycling.

Supplementary Note 3: phase transition during charge and its correlation with the charge photometry results.

To clarify the relationship between the particle cracking observed during charging in *operando* charge photometry and the corresponding crystallographic changes, it is essential to align the SOC between the charge photometry and *operando* PXRD results. While the cracking is noted during charging, directly correlating it using the charge voltage profile is challenging due to its lack of distinctive features, as demonstrated by the three-electrode voltage profiles (Figure S12a). Consequently, we utilise the reflection point in the discharge voltage profile, which is observable in both half-cell and full-cell voltage profiles, as indicated by the red arrow in Figures S12a-c. This point is also very close to point B where cracking is observed. We infer that the SOC at point B during the charge photometry experiment approximates $Na_{0.66}TMO_2$, corresponding to the SOC at which the reflection point appears in the full-cell voltage profile, as detailed in Supplementary Note 1.

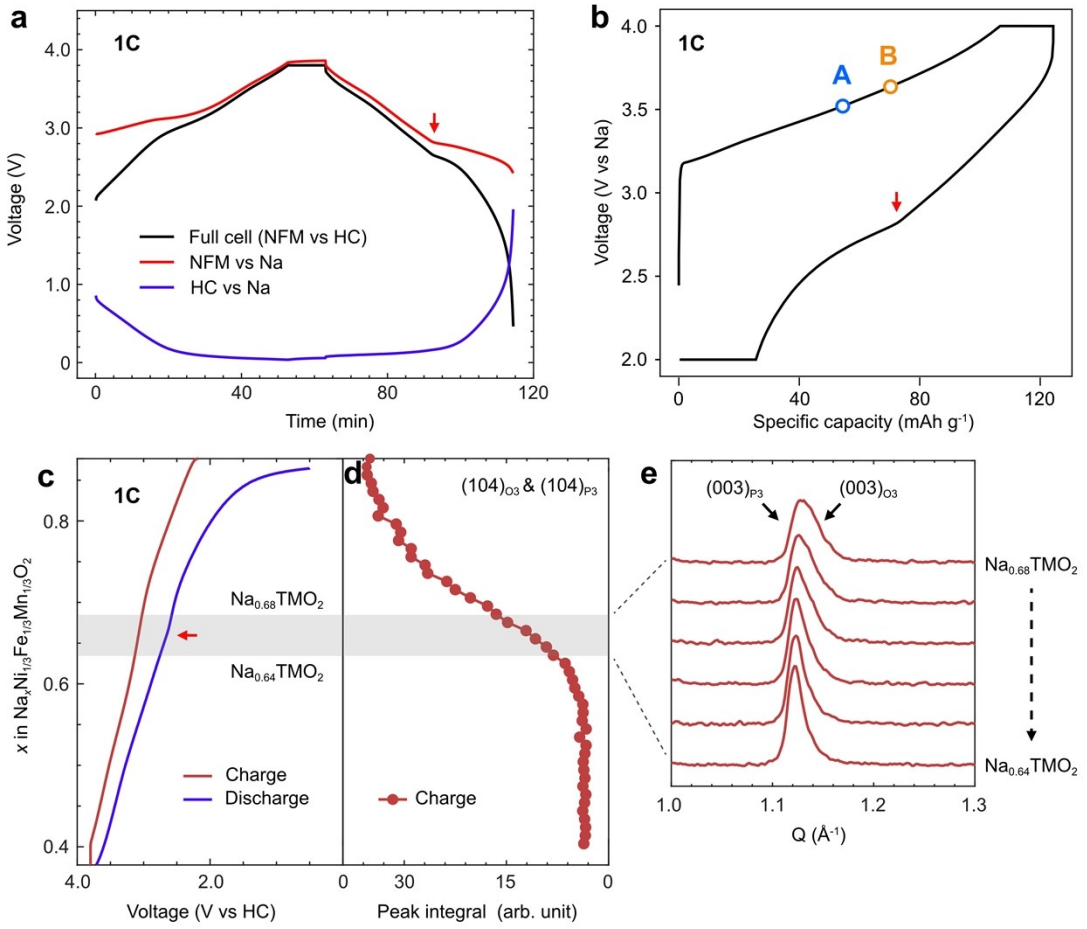

Figure S12. Correlating charge photometry with structural evolution. (a) Voltage profile of an NFM/HC full cell with a reference electrode of half de-sodiated Na $Na_3V_2(PO_4)_3$ (NVP).

The cathode and anode potentials are converted to values against Na by considering an equilibrium potential of the NVP reference electrode at 3.372 V vs Na/Na^+. (b) Voltage profile of an NFM/Na cell for the charge photometry experiment at 1C rate. (c) Comparison of the voltage profiles of the *operando* PXRD cell at 1C rate during both charge and discharge processes. The shaded region highlights the SOC range from $Na_{0.68}TMO_2$ to $Na_{0.64}TMO_2$. The red arrows in a, b and c indicate the reflection point in the voltage curve. (d) Changes in the integral of the (104) peak during charging. (e) Evolution of the (003) reflection peaks.

With this assignment, we investigate the structural changes occurring during charging, specifically within the SOC range of $Na_{0.68}TMO_2$ to $Na_{0.64}TMO_2$, as shown by the shaded area in Figures S12c and S12d. Specifically, we plotted the integral of the (104) signal for the O3 and P3 phases (Figure S12c) and examined the (003) peaks (Figure S12d) within this SOC range. The integral of the (104) peak demonstrates a gradual decrease as charging progresses from $Na_{0.68}TMO_2$ to $Na_{0.64}TMO_2$, indicating a reduction of the O3 phase and a corresponding increase in the P3 phase. This O3-to-P3 transition is further confirmed by the (003) reflection peak's shape (Figure S12e). Initially, at $Na_{0.68}TMO_2$, there is a clear $(003)_{O3}$ shoulder at higher Q values. As the transition advances, the peak becomes sharper and more symmetric, highlighting the P3 phase's dominance. Collectively, these analyses suggest that, at the SOC at point B during charging, the NFM cathode resides within the O3-P3 coexistence region, and the pronounced structural differences contribute to intra-granular cracking.

It is also noteworthy that the O3-P3 phase transition behaviour during charging and discharging differs to some extent at a 1C rate, as evidenced by the *operando* PXRD results (Figure 1b, Figures S4d and S12d). Specifically, the upper SOC limit of the two-phase coexistence region differs slightly: during discharge, it ends at approximately $Na_{0.66}TMO_2$, while during charge, it extends to approximately $Na_{0.64}TMO_2$. Moreover, the (003) peak is more distinctly separated during discharge compared to charge, indicating a larger difference in the *c* lattice parameter. These differences suggest that the phase transition mechanism requires further dedicated investigations, which is, however, beyond the scope of this work.

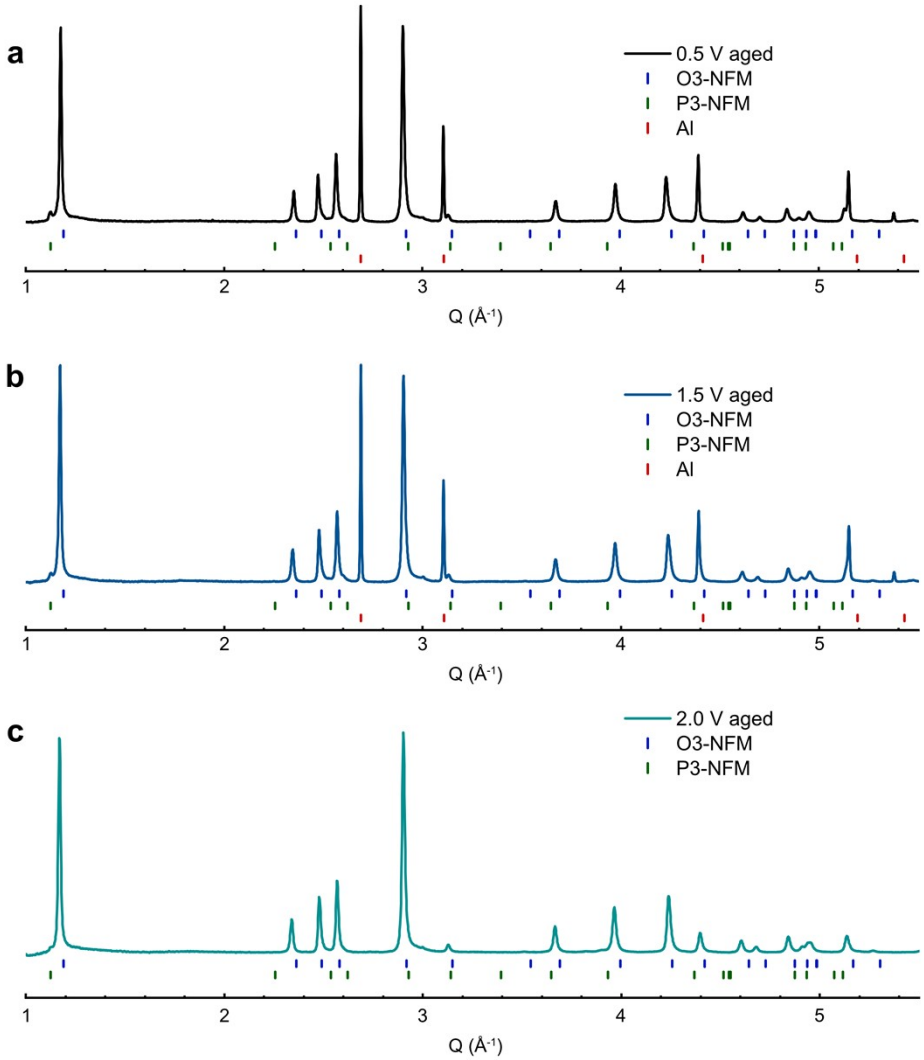

Figure S13. Ex-situ high-resolution synchrotron PXRD of cathodes from aged cells under various LCV conditions. (a) 0.5 V aged. (b) 1.5 V aged. (c) 2.0 V aged. The 2.0 V aged sample was a powder prepared by carefully scraping the NFM off the aluminium current collector, resulting in the absence of any detectable aluminium signal.

Supplementary Note 4: local structural change

To examine the alterations in local structure related to Fe migration, we consider three scenarios: no Fe migration, Fe migrating to the octahedral site in the Na layer, and Fe migrating to the tetrahedral site in the Na layer. The corresponding Rietveld refinements for each scenario are summarised below.

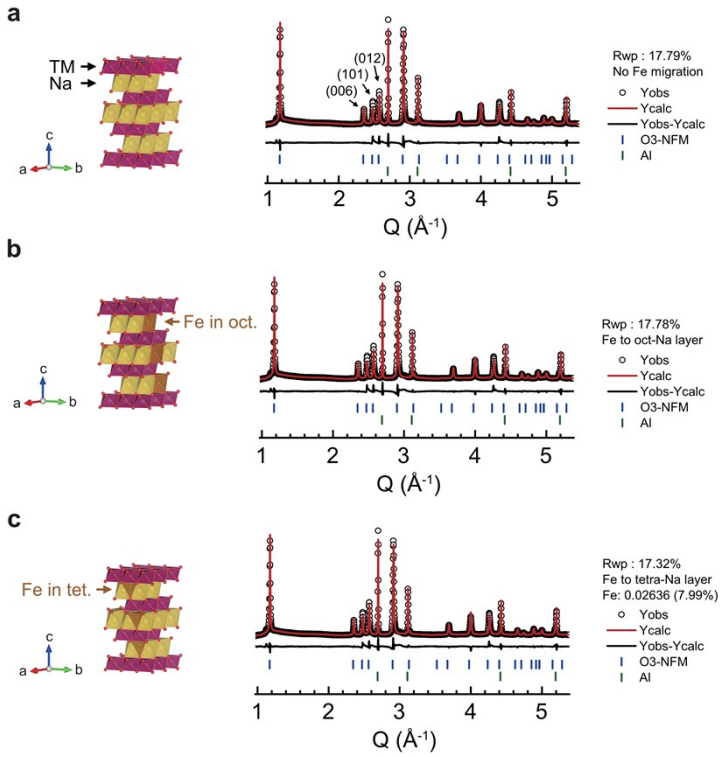

Figure S14. High-resolution synchrotron PXRD Rietveld refinement results of the 0.5 V aged LCV cell. (a) Refinement performed using the O3-phase model, assuming no Fe migration. (b) Refinement using the O3-phase model as the base framework, incorporating Fe in the octahedral sites of the Na layer to simulate Fe migration to these sites. (c) Refinement based on the O3-phase model, incorporating Fe in the tetrahedral sites to simulate Fe migration to these positions.

The differences in the (006), (101), and (012) reflections within the Q range of approximately between ~2.3 $Å^{-1}$ and ~ 2.7 $Å^{-1}$ reveal significant insights. The model, assuming no Fe migration, exhibits noticeable discrepancies between the experimental data and the calculated diffraction pattern. Incorporating the Fe-to-octahedral model does not enhance the refinement quality, with Fe occupancy in the Na octahedral layer calculated as zero, suggesting that this scenario is improbable. Conversely, when Fe is presumed to migrate to the tetrahedral site in the sodium layer, the fitting improves significantly. This is supported by the variations in peak

intensities and the fitting quality parameters. In this scenario, the Fe content is 0.027(2), corresponding to 8.0% of the total Fe present.

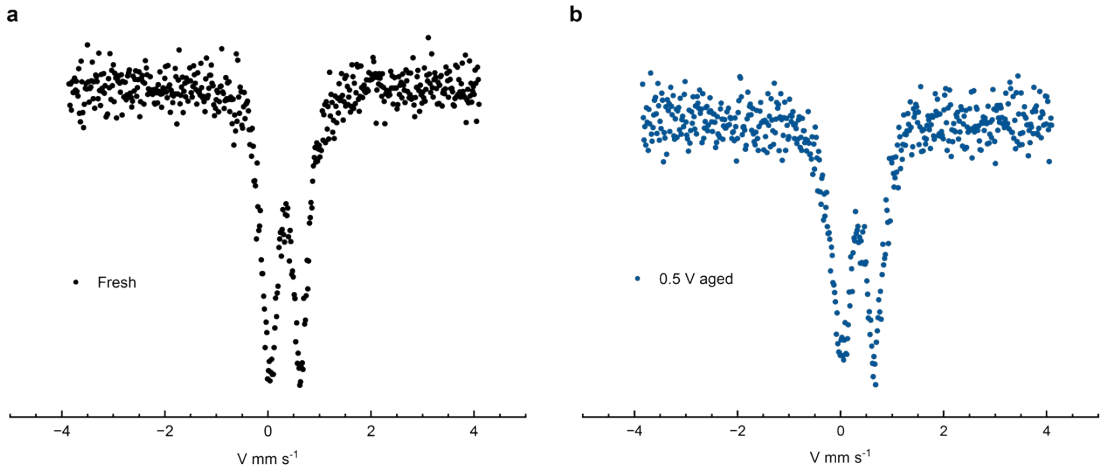

Figure S15. ^{57}Fe Mössbauer spectra of the fresh (a) and 0.5 V aged cathode (b).

We conducted ^{57}Fe Mössbauer spectroscopy measurements on fresh and 0.5 V aged samples to assess changes in the local Fe structure. Despite the relatively low signal-to-noise ratio, the spectra show no drastic alterations, corroborating the Rietveld refinement findings that only a minor amount of Fe migration occurs after extended cycling.

We further applied the Fe-to-tetrahedral model for refinement against the diffraction patterns of the 1.5 V and 2.0 V aged samples. The resulting Fe content in the tetrahedral sites was 0.026(2) and 0.024(2), respectively, indicating no significant difference from the 0.5 V sample. These results suggest that Fe migration is not the primary factor influencing the varied ageing behaviour of the NFM cathode at different LCVs.

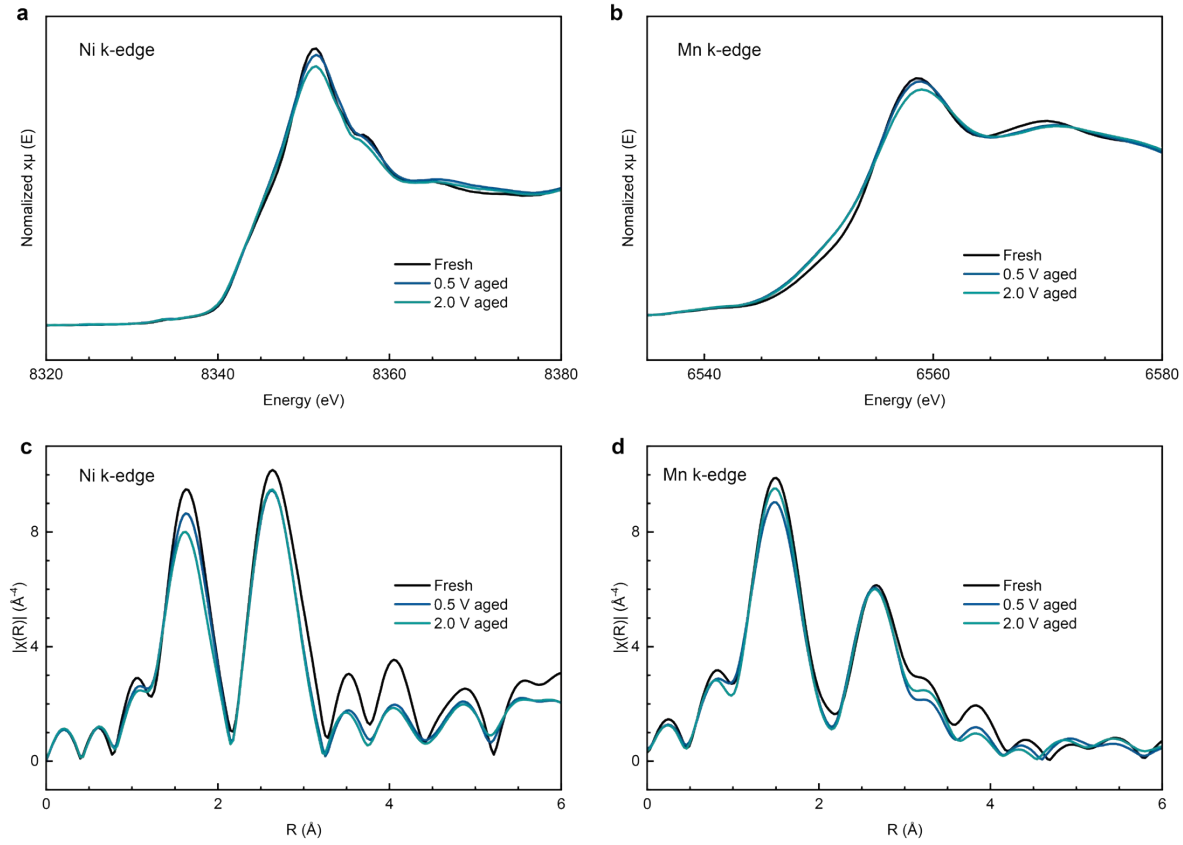

Figure S16. X-ray absorption spectroscopy (XAS) analysis of fresh and aged samples. (a-d) Normalised Ni K-edge (a) and Mn K-edge XANES spectra (b) for fresh, 0.5 V aged, and 2.0 V aged samples and corresponding Fourier-transformed EXAFS spectra (c, d).

Table S2. XPS elemental composition analysis of fresh and aged samples.

Sample	C/at.%	F/at.%	O/at.%
Fresh	69.06	25.03	5.91
0.5 V aged	51.14	18.59	30.27
2.0 V aged	52.72	23.26	24.02

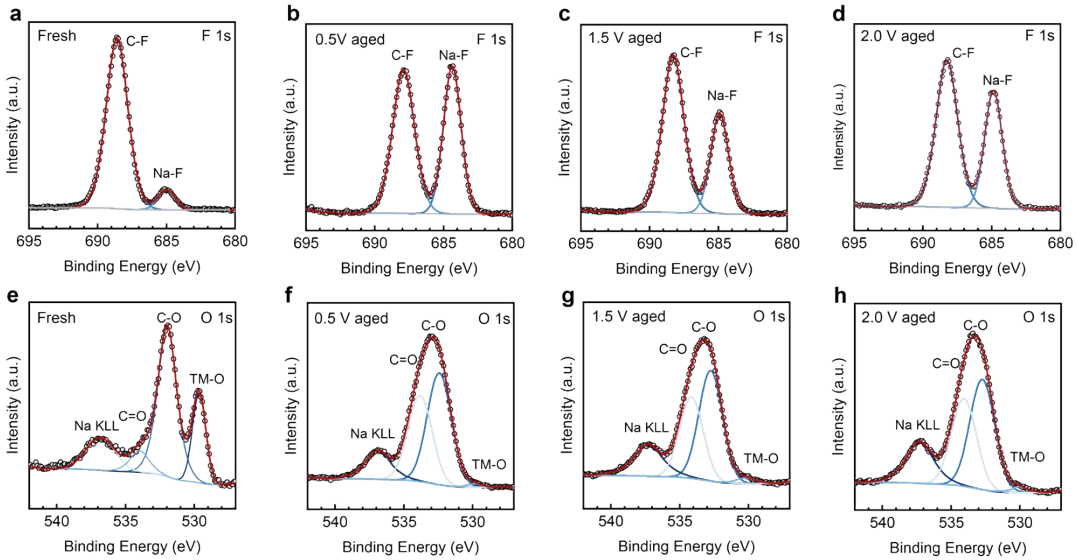

Figure S17. XPS analysis of F 1s and O 1s spectra for fresh and aged samples. (a-d) XPS analysis of F 1s spectra for fresh (a), 0.5 V aged (b), 1.5 V aged (c), and 2.0 V aged (d) samples. (e-f) XPS analysis of O 1s spectra for fresh (e), 0.5 V aged (f), 1.5 V aged (g), 2.0 V aged (h) samples.

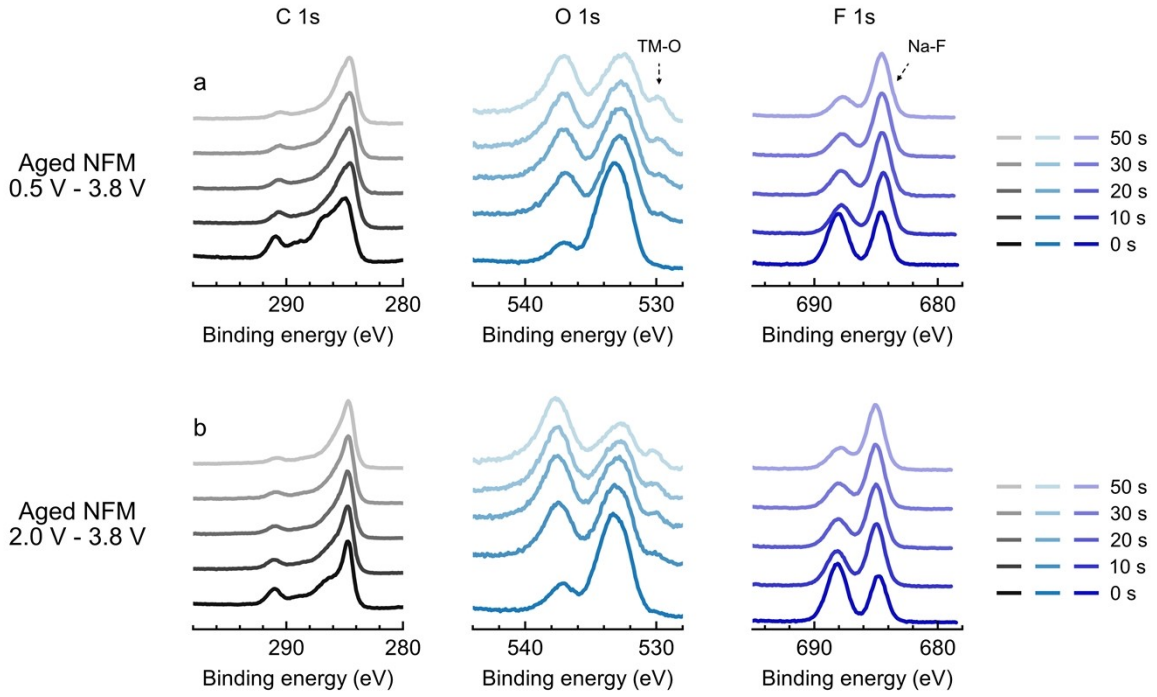

Figure S18. XPS depth profiling. C 1s, O 1s, and F 1s XPS spectra for 0.5 V aged NFM (a) and 2.0 V aged NFM (b) after 1,000 ageing cycles, after 0, 10, 20, 30, and 50 s sputtering, respectively.

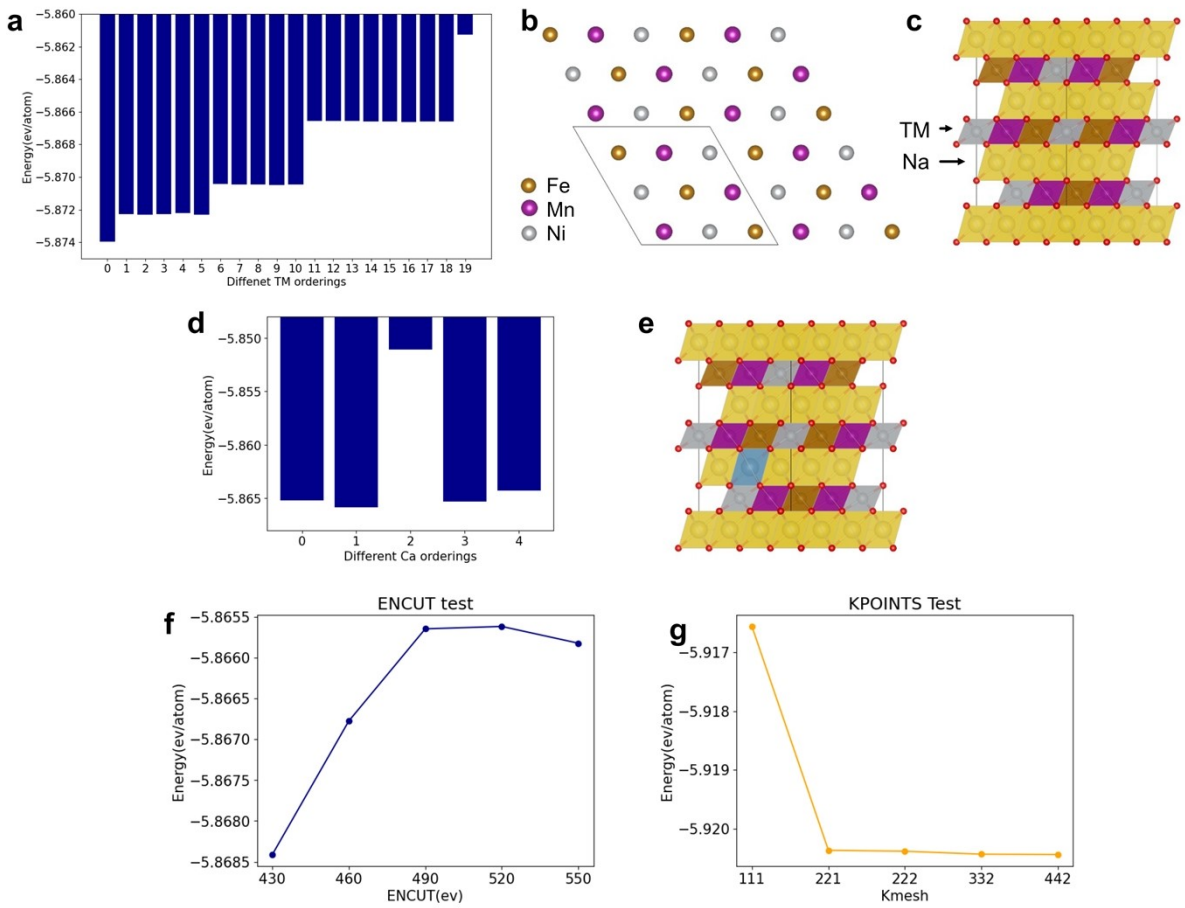

Figure S19. Calculation results for different TM and Na/Ca-vacancy orderings. (a) Energies for structures with different TM orderings. (b-c) Structural illustrations for the TM ordering with the lowest energy. (d) Energies for structures with different Na/Ca-vacancy orderings. (e) Structural illustrations for the Na/Ca-vacancy ordering with the lowest energy. (f) ENCUT convergence test plot. (g) k-points convergence test plot.

Table S3. Comparison of calculated and experimental values of NFM and NFM-Ca systems.

O3-NFM				
Na removal	10	8	6	4
Na content (calculation)	0.62963	0.703704	0.777778	0.851852
c-parameter (Å; calculation)	16.57206	16.46617	16.33781	16.24981
Na content (experiment)	0.66935	0.70288	0.77664	0.85041
c-parameter (Å; experiment)	16.45283	16.36635	16.24667	16.11633
Δ (Å)	-0.11923	-0.09982	-0.09114	-0.13348
O3-NFM-Ca				
Na removal	10	8	6	4
Na content (calculation)	0.55556	0.62963	0.703704	0.77778
c-parameter (Å; calculation)	16.56458	16.47647	16.37332	16.27371
Na content (experiment)	0.60028	0.63039	0.70400	0.77760
c-parameter (Å; experiment)	16.50146	16.33534	16.26299	16.15759
Δ (Å)	-0.06312	-0.04458	-0.11033	-0.11612

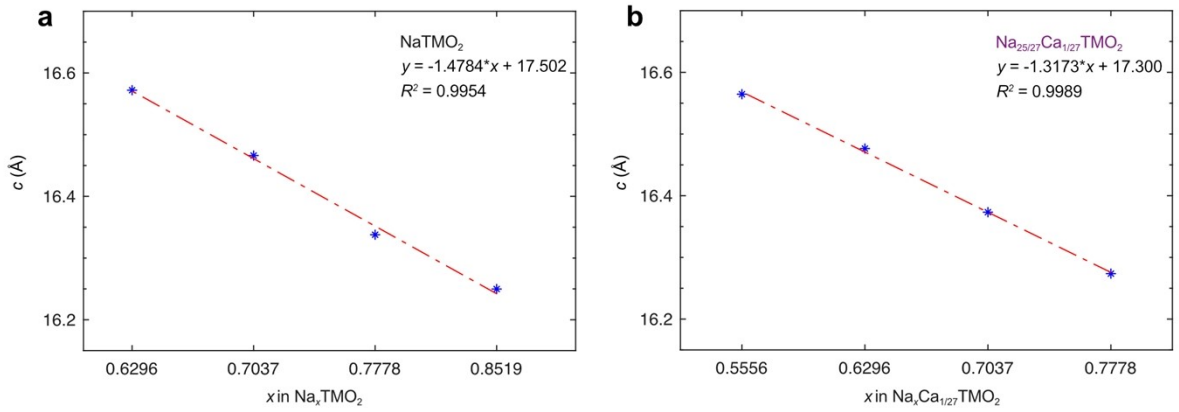

Figure S20. Linear fitting analyses of the changes in the c lattice parameter for both Ca-free and Ca-substituted NFM cathodes. The slopes were further normalised relative to specific capacities by dividing them by their corresponding theoretical capacities of 240.385 mAh g^{-1} for Ca-free NFM and 240.883 mAh g^{-1} for Ca-substituted NFM. This normalisation results in rates of 6.15×10^{-3} Å per mAh g^{-1} for Ca-free NFM and 5.47×10^{-3} Å per mAh g^{-1} for Ca-substituted NFM.

Table S4. Stoichiometry from ICP-OES results of NFM, NFM-Ca2 and NFM-Ca4 samples. The Na content for the NFM-Ca2 and NFM-Ca4 is slightly higher than the theoretical stoichiometries. This is attributed to the fact that an additional 3.0 wt% of Na was added during the synthesis of these two materials.

Sample	Na	Ca	Ni	Fe	Mn
NFM111-Powder	1.004	/	0.338	0.334	0.328
$Na_{0.96}Ca_{0.02}$NFM111-Powder	1.006	0.0215	0.333	0.339	0.328
$Na_{0.92}Ca_{0.04}$NFM111-Powder	0.960	0.0402	0.332	0.339	0.329

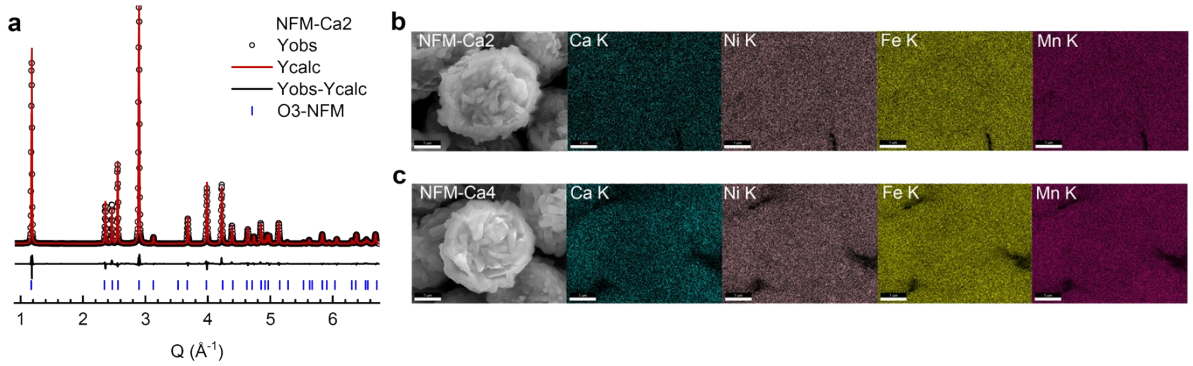

Figure S21. Ca-doped polycrystalline materials. (a-c) High-resolution synchrotron PXRD (a) and EDS elemental mapping of the NFM-Ca2 sample (b), along with EDS elemental mapping of the NFM-Ca4 sample (c).

Sample group：$R3m$ α=β=90°，γ=120°							
Sample	c/Å	a/Å	vol/Å^3	Z_O	Na layer (Å)	Rwp/%	GOF
NFM	15.9967(4)	2.9852(0)	123.457(6)	0.23257(2)	3.2238	11.74	0.6101
NFM-Ca2	15.9912(4)	2.9863(0)	123.504(5)	0.23273(1)	3.2175	10.45	0.5338
NFM-Ca4	15.9969(3)	2.9858(0)	123.509(4)	0.23283(1)	3.2155	9.85	0.5087

Table S5. Rietveld refinement results of NFM, NFM-Ca2 and NFM-Ca4 powder.

Supplementary Note 5. Analysis of calcium distribution.

First, Calcium presence is verified through Inductively Coupled Plasma (ICP) analysis, confirming the existence of Ca ions in the NFM-Ca2 and NFM-Ca4 samples (Table S4). In the subsequent discussion, we examine the characteristics of calcium. We hypothesise that calcium may exist in one of two forms: as surface residue in the form of calcium carbonate ($CaCO_3$) or incorporated into the oxide lattice as a dopant. We conducted Calcium K-edge X-ray absorption spectroscopy on the pristine NFM-Ca4 sample and compared it with a calcium carbonate reference. The X-ray absorption near edge structure (XANES) spectra (Figure S22) show similar edge positions at a normalised absorption of 0.5, indicating that both forms of calcium exhibit a similar nominal valence state of +2. Furthermore, the near-edge structure shows significant variations, indicating that the Ca is highly likely to exist as a dopant in the layered oxide lattice instead of a $CaCO_3$ impurity. This is further supported by high-resolution synchrotron PXRD, which shows no impurity phases are detected in the pristine NFM-Ca4 sample (Figure 4b).

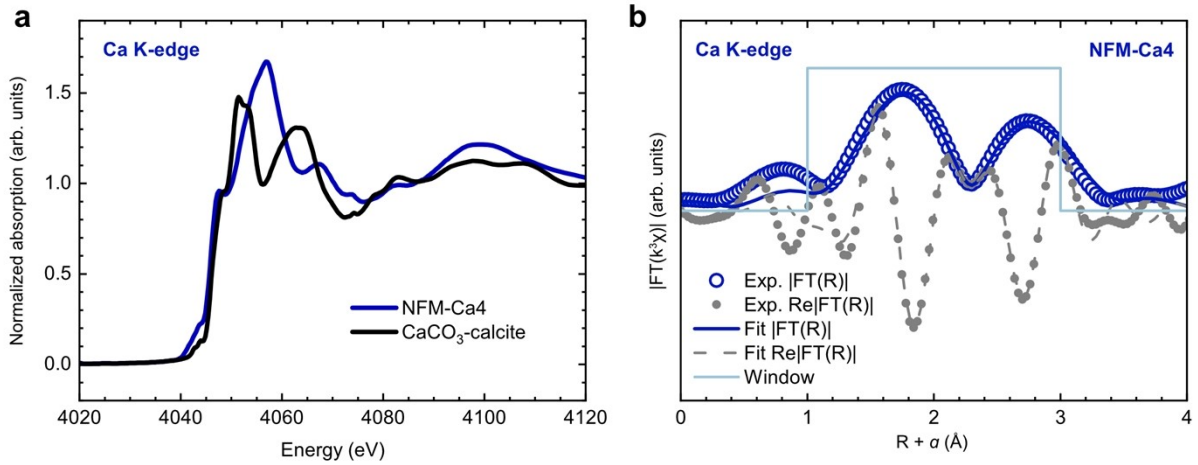

Figure S22. XAS results. (a) Ca K-edge XANES spectra for pristine NFM-Ca4 and $CaCO_3$. (b) The EXAFS and curve fit for pristine NFM-Ca4 are shown in R-space (FT magnitude and imaginary components). The EXAFS data is k^3-weighted and not phase-corrected.

Assuming Ca^{2+} serves as a dopant ion, we conducted a fitting analysis of the extended X-ray absorption fine structure (EXAFS) to assess how calcium is distributed within the oxide lattice. We utilised two initial models where Ca occupies octahedral positions in either the Na or transition metal (TM) layers, summarising the fitting parameters in Table S6. Notably, despite starting from different models, both fitting analyses yield remarkably similar results. The parameters for the Ca in the TM layer model show significant changes from the initial ones.

Specifically, the Ca-O and Ca-TM path lengths are 2.30/2.30 Å and 3.28/3.29 Å, respectively (column *R* in Table S6). These lengths agree closely with the Na-O and Na-TM bond lengths, 2.36 Å and 3.18 Å, derived from lattice parameters through Rietveld refinements with high-resolution synchrotron PXRD results (Table S7).

Table S6. Fitting parameters for the Ca K-edge EXAFS of the pristine NFM-Ca4. S_0^2 was fixed at 0.62. ΔE_0 was refined as a global fitting parameter, resulting in a value of 0.05 eV. The data fitting range was set to $3.0 \leq k \leq 8.0$ Å^{-1} and $1.0 \leq R \leq 3.0$ Å. The R factors for these two fittings are 3.37% for the Ca in the Na layer and 3.70% for the Ca in the TM layer models, respectively. Note column d represents the initial path distances obtained from the crystal structure.

Initial model	Path	*d* (Å)	*N*	*R* (Å)	σ^2 (Å^2)
Ca in Na layer	Ca-O	2.348	6	2.30(5)	0.003(1)
	Ca-Na	2.986	6	2.97(1)	0.005(2)
	Ca-TM	3.175	6	3.28(2)	0.007(2)
Ca in TM layer	Ca-O	2.029	6	2.30(5)	0.003(8)
	Ca-Na	3.175	6	2.98(2)	0.005(5)
	Ca-TM	2.986	6	3.29(1)	0.007(5)

Table S7. Structural parameters of NFM, NFM-Ca2, and NFM-Ca4 powder obtained from Rietveld refinement against high-resolution synchrotron PXRD patterns.

Sample	*a* (Å)	*c* (Å)	Z_O	Na-O (Å)	TM-O (Å)	Na-TM (Å)
NFM	2.9852(0)	15.9967(4)	0.23257(2)	2.360	2.020	3.175
NFM-Ca2	2.9863(0)	15.9912(4)	0.23273(1)	2.358	2.022	3.174
NFM-Ca4	2.9858(0)	15.9969(3)	0.23283(1)	2.357	2.023	3.175

The presence of calcium in the Na layer is further confirmed by additional DFT calculations. We calculated the reaction energies of doping of Ca ions to different sites (Na, Ni, Fe, Mn) in a grand canonical ensemble open to O_2 gas, consistent with the experimental synthesis conditions. The corresponding reaction equations are: (1-4).

$$5Na_2O + CaO + 4NiO + 2Fe_2O_3 + 4MnO_2 = [CaNa_{10}]Ni_4Fe_4Mn_4O_{24} \quad (1)$$

$$6Na_2O + CaO + 3NiO + 2Fe_2O_3 + 4MnO_2 = Na_{12}[CaNi_3Fe_4Mn_4]O_{24} \quad (2)$$

$$6Na_2O + CaO + 4NiO + 3/2Fe_2O_3 + 4MnO_2 + 1/4O_2 = Na_{12}[CaNi_4Fe_3Mn_4]O_{24} \quad (3)$$

$$6Na_2O + CaO + 4NiO + 2Fe_2O_3 + 3MnO_2 + 1/2O_2 = Na_{12}[CaNi_4Fe_4Mn_3]O_{24} \quad (4)$$

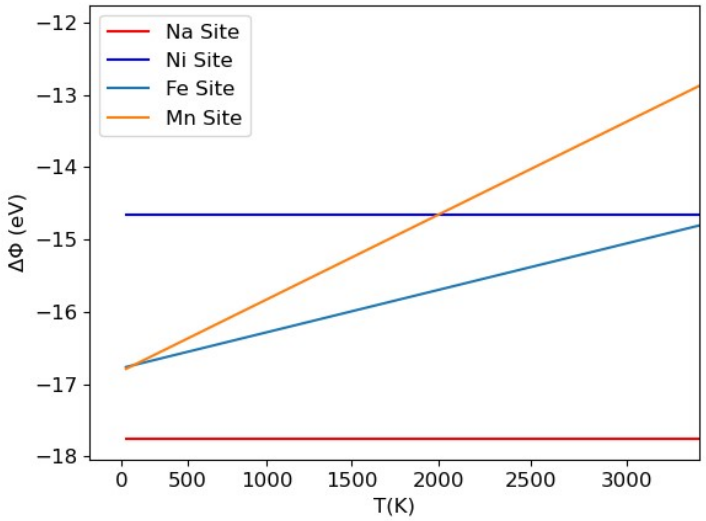

Figure S23. Energies at different temperatures for different Ca-doped site systems of the giant canonical system.

Finite-temperature reaction energies were evaluated by including the entropy of O_2 gas while assuming that the entropy change (ΔS) between the solid phases is negligible, as is common for equilibria involving oxygen. The calculation results in Figure S23 show that Ca ions occupying the Na site have the most negative reaction energy at all temperatures. This indicates that doping Ca into the Na site is thermodynamically favourable in high-temperature solid-state reactions, which is consistent with experimental results.

Collectively, these results confirm that Ca^{2+} is distributed in the NFM oxide lattice and occupies the Na sites, serving as a dopant. We attribute this preference to the similar ionic radii of Ca^{2+} (1.0 Å) and Na^{+} (1.02 Å), which are much larger than those of Ni^{2+} (0.69 Å), Fe^{3+} (0.64 Å), and Mn^{4+} (0.53 Å), effectively eliminating the chance of Ca ions taking up transition metal sites due to steric hindrance.

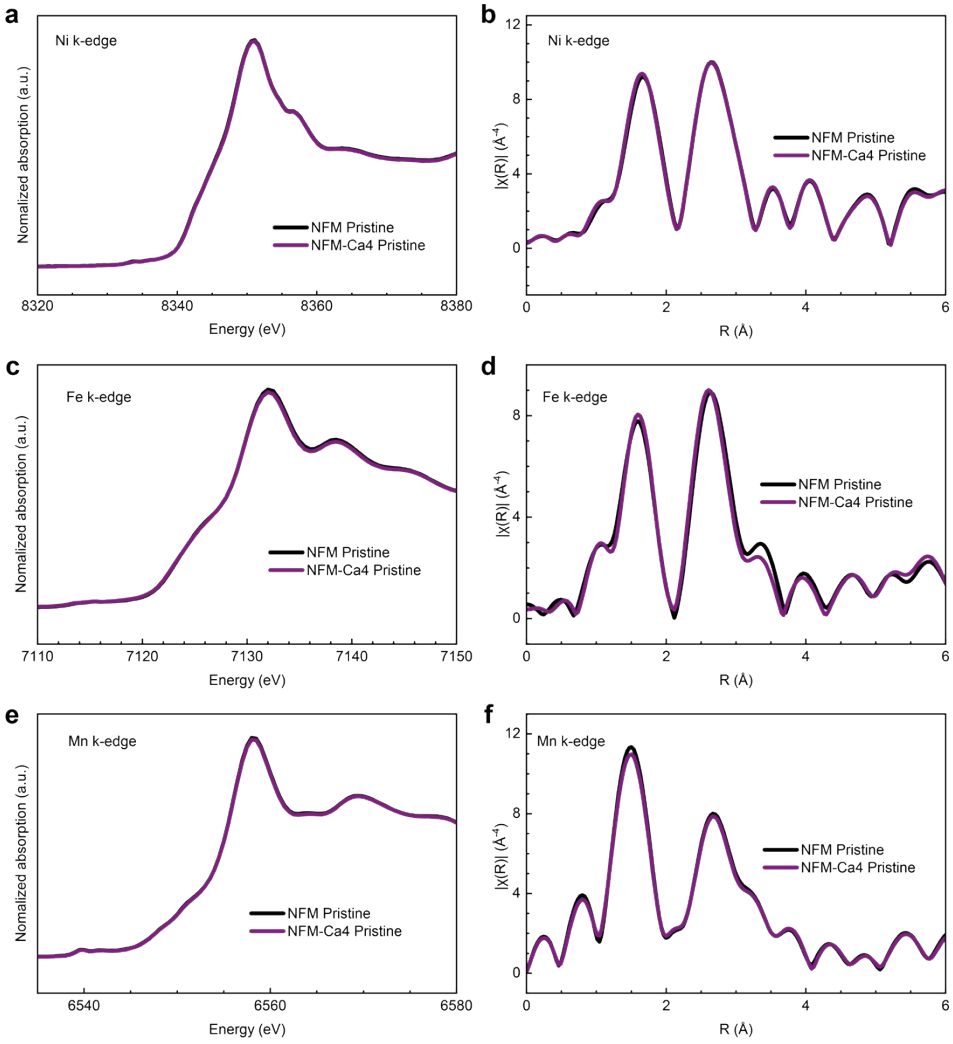

Figure S24. XAS spectra for pristine NFM and NFM-Ca4. (a-b) Ni K-edge XANES (a) and EXAFS shown in R-space (b). (c-d) Fe K-edge XANES (c) and EXAFS shown in R-space (d). (e-f) Mn K-edge XANES (e) and EXAFS shown in R-space (f).

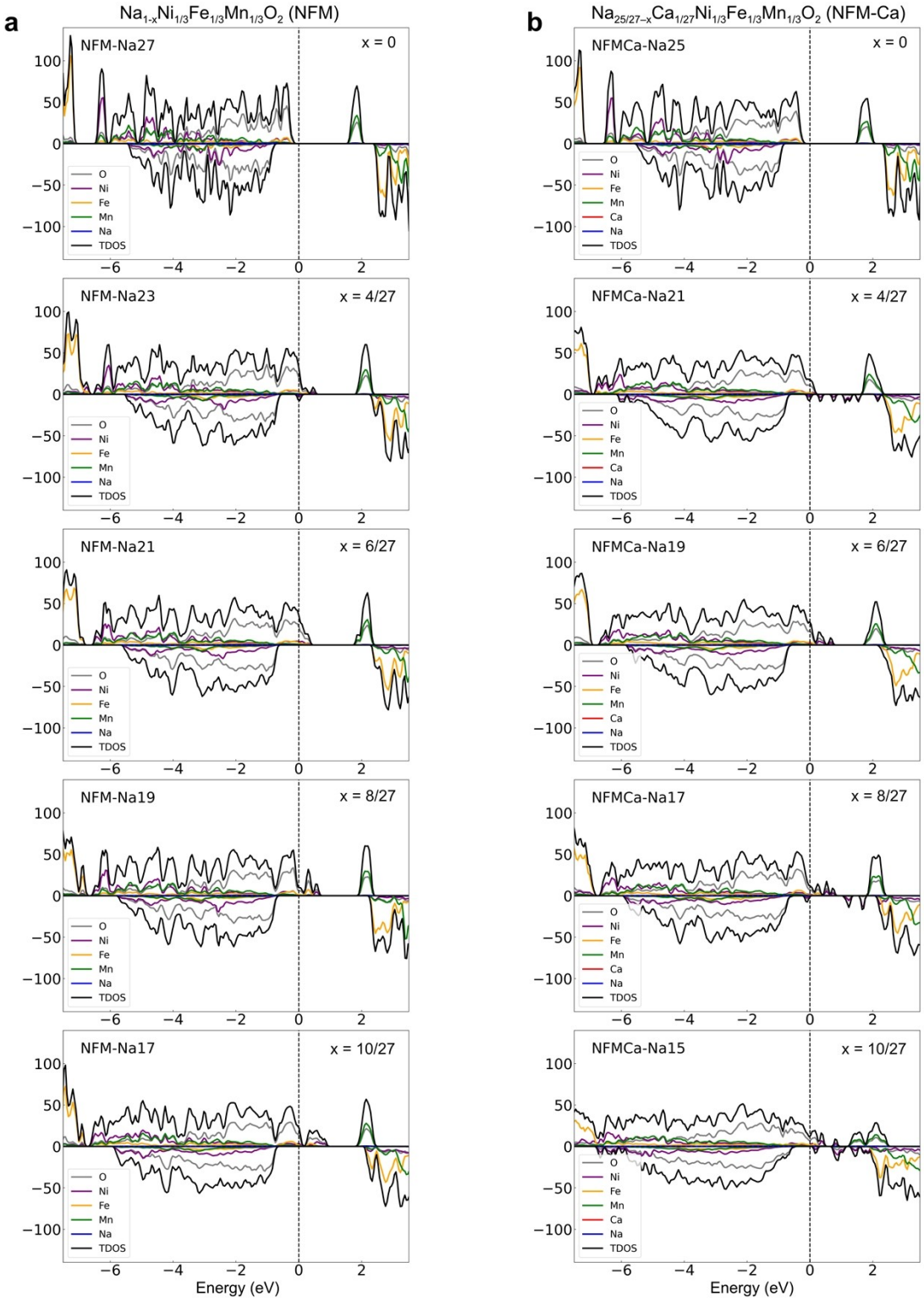

Figure S25. Density of states (DOS) plots for the NFM (a) and NFM-Ca (b) systems at various SOCs. The results, listed from top to bottom, correspond to x=4/27, 6/27, 8/27, and 10/27, respectively.

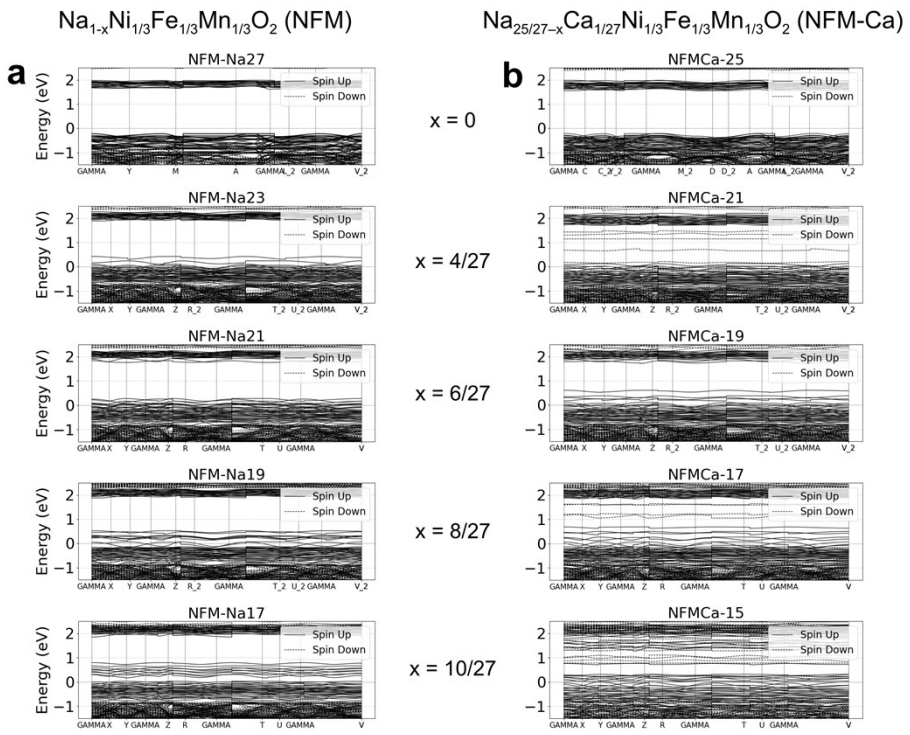

Figure S26. Band structure plots for the NFM (a) and NFM-Ca (b) systems at various SOCs. The results, listed from top to bottom, correspond to x=4/27, 6/27, 8/27, and 10/27, respectively.

Table S8. Calculation of Bader charge for NFM and NFM-Ca systems.

Structure	Central atom	Electronic changes	Electronic changes - O
NFM (Na27)	Na	-0.83719	1.20827
NFM-Ca (Na25)	Ca	-1.518407	1.22074

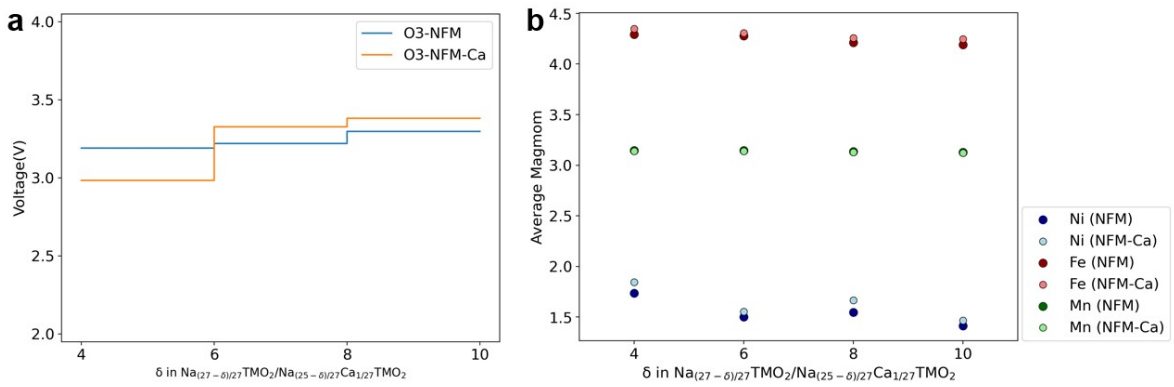

Figure S27. (a) Calculated voltages for the NFM system and the NFM-Ca system for a partial SOC range. (b) Variation of magnetic moments of transition metal elements with different Na contents for NFM and NFM-Ca systems.

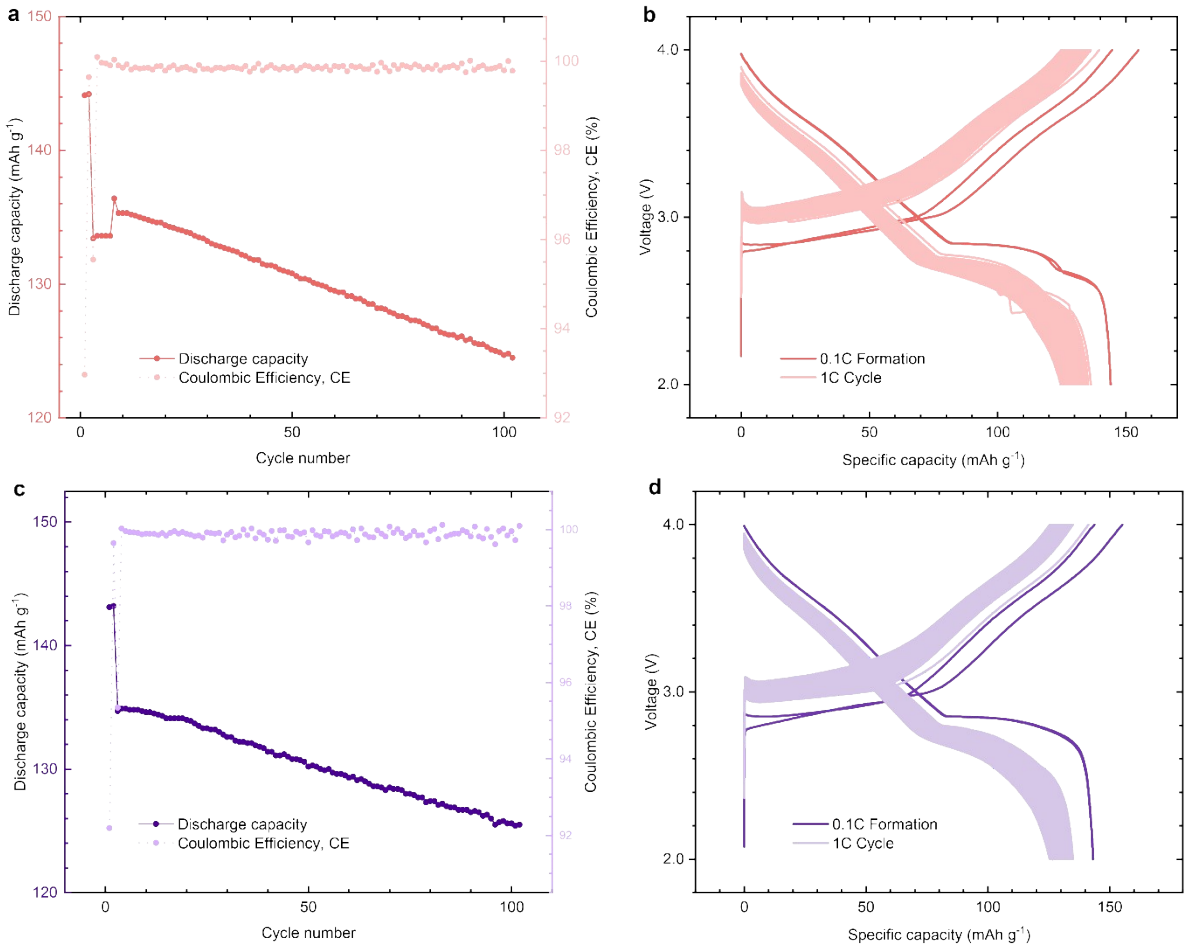

Figure S28. Electrochemical performance of NFM-Ca2/Na and NFM-Ca4/Na half-cell. (a-b) Cycling performance of NFM-Ca2/Na half-cell at 1C rate after two formation cycles at 0.1C rate (a) and voltage profiles (2.0 V – 4.0 V) during cycling (b). (c-d) Cycling performance of NFM-Ca4/Na half-cell at 1C rate after two formation cycles at 0.1C rate(c) and voltage profiles (2.0 V – 4.0 V) during cycling (d).

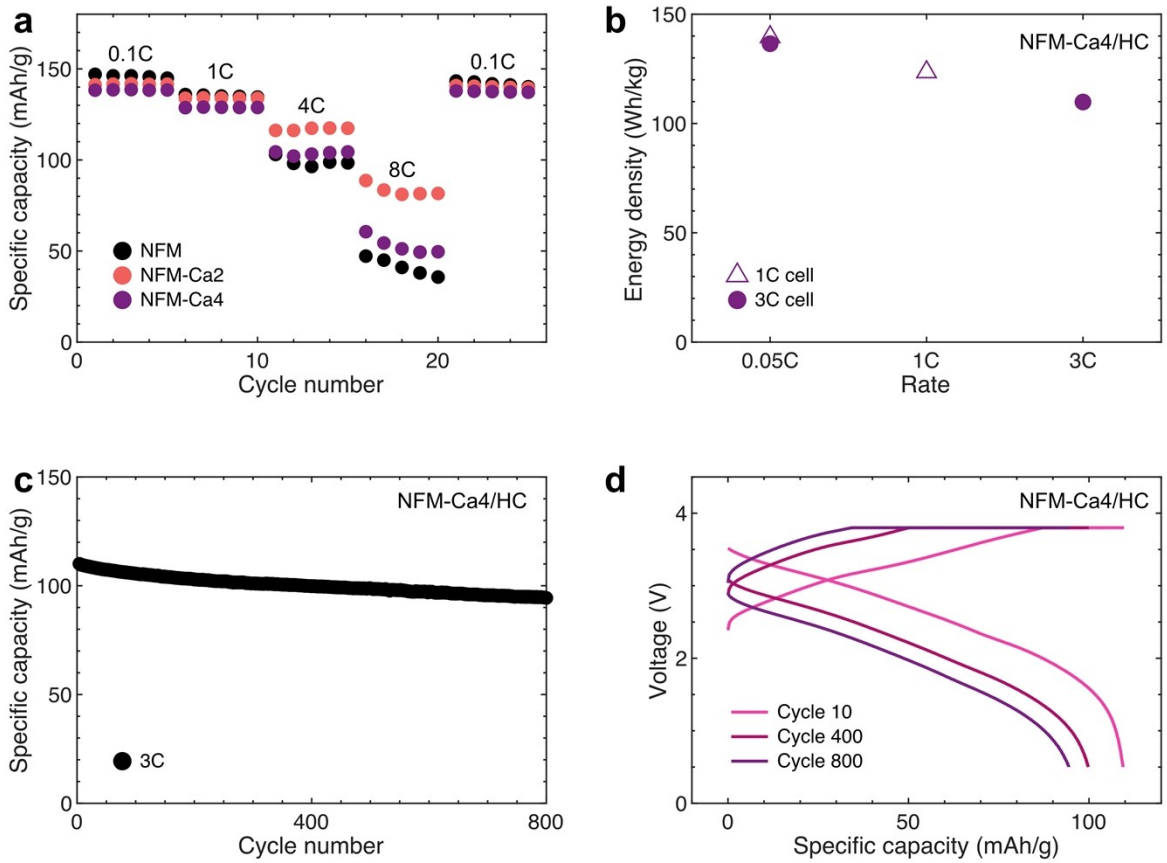

Figure S29. Rate capability characterisations. (a) Rate capability tests in half cells for NFM, NFM-Ca2, and NFM-Ca4 at 0.1C, 1C, 4C, and 8C, respectively. The voltage window is 2.0 – 4.0 V. (b) Energy density of NFM-Ca4/HC full cells at 0.05C, 1C, and 3C. (c) Capacity retention of NFM-Ca4/HC full cell at 3C. (d) Voltage profiles for the NFM-Ca4/HC full cell at 3C during cycle 10, 400 and 800. The voltage window for the full cell results shown in b-d is 0.5 – 3.8 V.

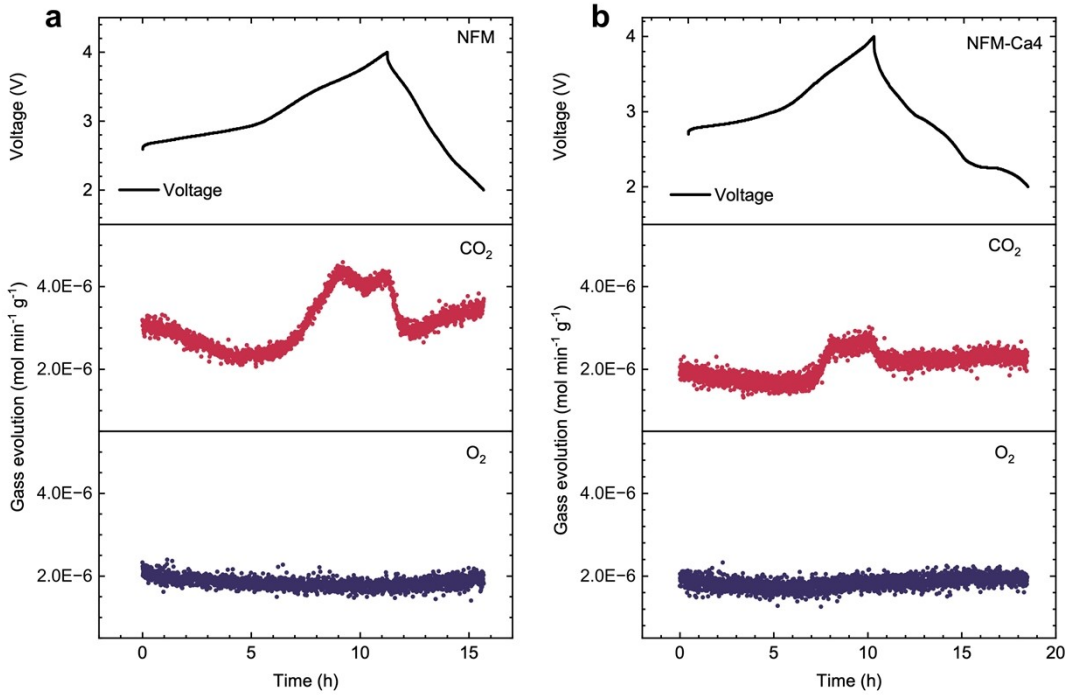

Figure S30. DEMS results for NFM (a) and NFM-Ca4 (b) during the first cycle.

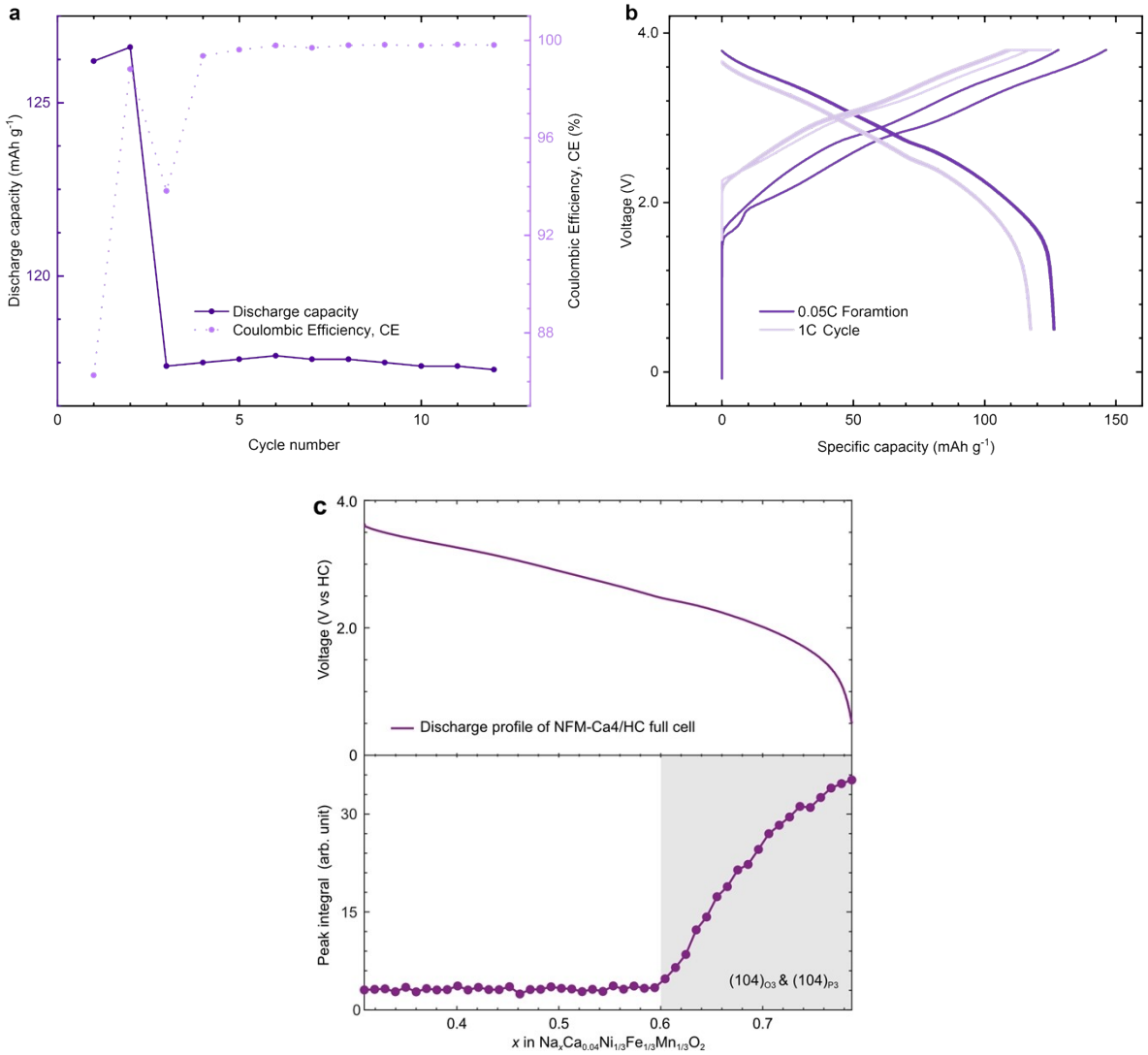

Figure S31. Electrochemical performance of NFM-Ca4/HC full cell. (a-b) Cycling performance of NFM-Ca4/HC full cell at 1C rate after two formation cycles at 0.05C rate(a) and voltage profiles (0.5 V – 3.8 V) during cycling (b). (c) The discharge profile of NFM-Ca4/HC full cell and the corresponding peak integral of the $(104)_{O3}$ and $(104)_{P3}$ region.

Table S9. Comparison of Na layer changes between NFM and NFM-Ca systems near the phase transition point.

Structure	$NFM\text{-}Na_{17/27}$	$NFMCa\text{-}Na_{15/27}$
P3-Na Layer	3.448	3.544
O3-Na Layer	3.407	3.550
Δ	1.20%	0.17%

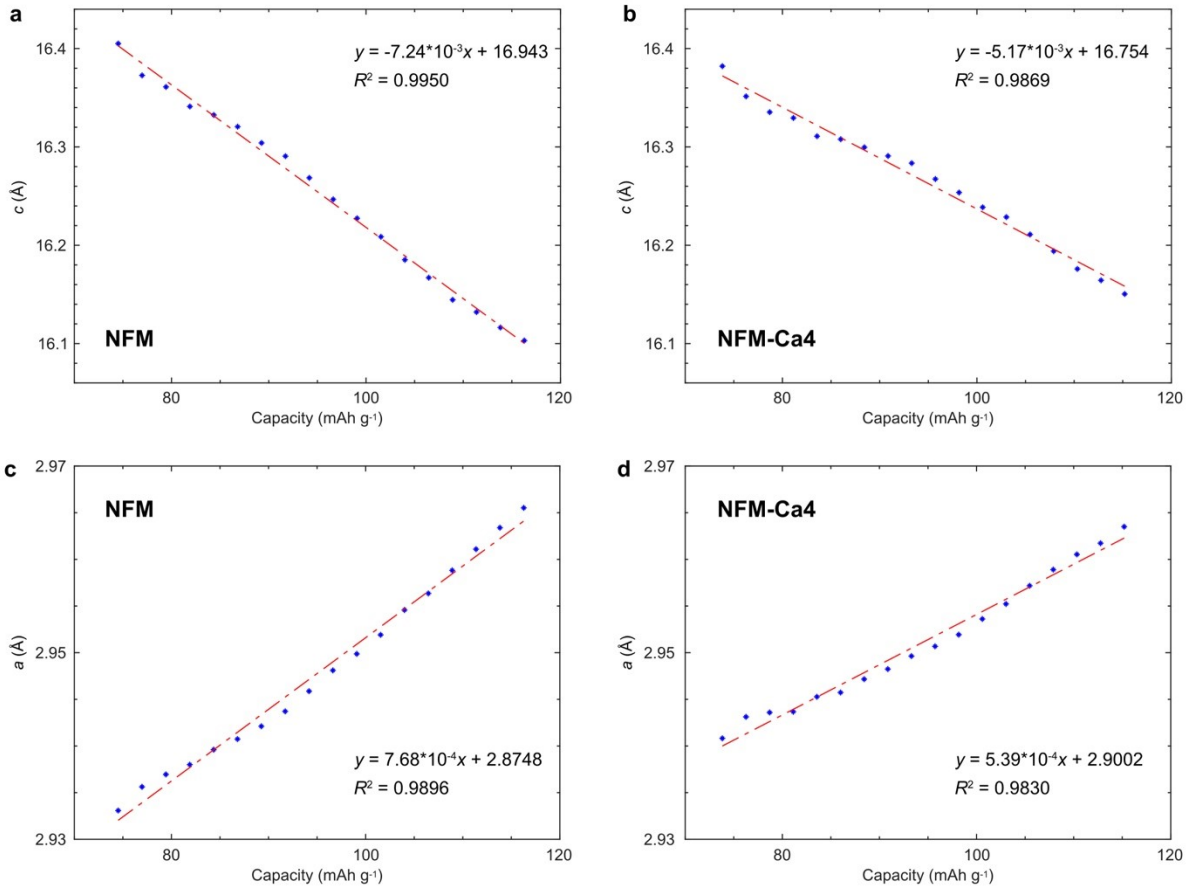

Figure S32. Linear fitting analysis of lattice parameter evolution. (a-b) Linear fitting results of the change in the *c* parameter for NFM (a) and NFM-Ca4 (b) cathode materials. (c-d) Linear fitting results of the change in the *a* parameter for NFM (c) and NFM-Ca4 (d) cathode materials.

Supplementary Note 6. Estimation of full cell energy density.

Note that our full cells are single-layer pouch cells with a relatively low areal loading of the cathode and anode (~1 mAh cm^{-2} for the cathode) compared to typically industry-level cells. Therefore, calculating the energy density by normalising the energy with the mass of our single-layer pouch cell does not accurately reflect the true properties of the cathode materials. Consequently, we employ an A5-sized (15 Ah) pouch full-cell energy density prediction model validated by Faradion[11]. Table S10 demonstrates the typical analysis for the NFM-Ca4/hard carbon full cell using the specific capacity and average discharge voltage values of our NFM-Ca4/hard carbon full cell, whose electrochemical performance is also shown in Figure 5a. This leads to a gravimetric energy density of 129.7 Wh kg^{-1} and a volumetric energy density of 336.2 Wh L^{-1} (estimated using capacity and voltage values obtained at 1C).

Table S10. Calculations of gravimetric and volumetric energy density.

Gravimetric Energy Density Analysis of 15 Ah Pouch Cell	
Parameter	Specification & Value
Pouch Cell Dimension	148 mm × 210 mm (A5)
Electrode Dimensions	Cathode: 189 mm × 99 mm Anode: 190 mm × 100 mm
Tab Dimension	0.1 mm × 6 mm × 46 mm
Separator Dimension	195 mm × 105 mm
Number of Layers	Cathode: 18 Anode:18 Sparator:35
N/P Ratio	1.12
Active Material Areal Loading	Cathode: 20 mg cm^{-2} Anode: 10.826 mg cm^{-2}
Electrode Material Mass	Cathode: 145.53 g (90:5:5) Anode: 74.63 g (95:5)
Electrolyte	95.6 g
Current Collector & Auxiliary Material Mass	Cathode/Anode Al foil: 19 g Separator: 7.6 g Tabs (two): 0.17 g Pouch Aluminum-Plastic Film: 7.46 g
Average Discharge Voltage	2.8488 V
Specific Discharge Capacity (0.5 V-3.8 V,1 C)	121.64 mAh g^{-1}
Total Cell Power	45.39 Wh
Total Cell Mass	0.350 kg
Energy Density	129.7 Wh kg^{-1}

Volumetric Energy Density Analysis of a 15 Ah Pouch Cell	
Parameter	Value
Cathode material compaction density	3.3 g cm^{-3}
Cathode material layer thickness	2.1 mm
Anode material compaction density	0.98 g cm^{-3}
Anode material layer thickness	3.8 mm
Current collector (Al foil) thickness	0.36 mm (single-layer thickness: 0.01 mm)
Separator thickness	0.7 mm (single-layer thickness: 0.02 mm)
Pouch cell aluminium -laminated film thickness	0.134 mm (single-layer thickness: 0.067 mm)
Total volume	134.78 cm^3 (0.135 L)
Volumetric energy density	336.2 Wh L^{-1}

Based on this method, we further calculated the energy density of four important cells: NFM/HC, NFM-Ca2/HC, and NFM-Ca4/HC (cycling results shown in Figure 5a), using a voltage window of 0.5 – 3.9 V, and NFM-Ca4/HC with a voltage window of 0.5 – 3.8 V (cycling results shown in Figure S33). The results are summarised in Table S11. It is clear that the energy density decreases only marginally as the calcium content increases, reducing by approximately 2.5% for the Ca4 cell compared to the Ca-free cell. Additionally, lowering the upper cutoff voltage further enhances cycling stability, resulting in 80% capacity retention for over 1,300 cycles, as the reviewer refers to, which decreases the energy density by about 4.7% compared to the same cell chemistry cycled up to 3.9 V. As such, we demonstrate that calcium substitution drastically enhanced cycling stability with a limited sacrifice in energy density.

Table S11. Gravimetric and volumetric energy densities of full cells.

Voltage window (V)	Cell chemistry	Gravimetric energy density (Wh kg^{-1})	Volumetric energy density (Wh L^{-1})
0.5 - 3.9 V	NFM/HC	133.0	347.6
	NFM-Ca2/HC	131.0	339.9
	NFM-Ca4/HC	129.7	336.2
0.5 - 3.8 V	NFM-Ca4/HC	123.6	316.7

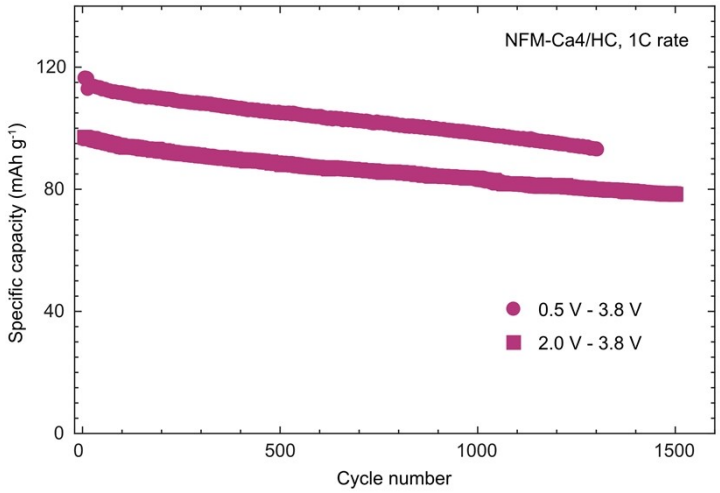

Figure S33. Capacity retention of NFM-Ca4/HC full cells cycled with voltage windows of 0.5 V – 3.8 V and 2.0 V – 3.8 V.

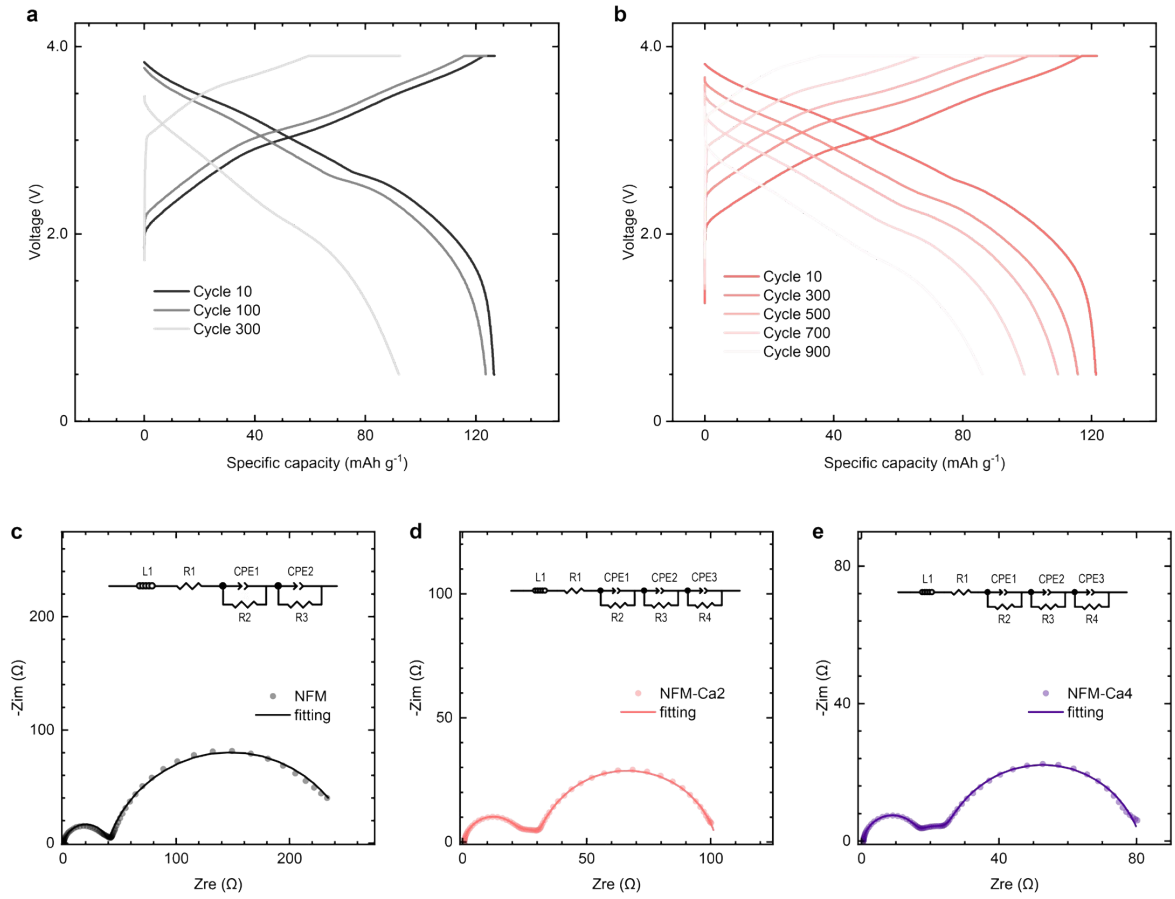

Figure S34. Electrochemical performance and EIS analysis of NFM/HC, NFM-Ca2/HC and NFM-Ca4/HC full cells after 450 cycles. (a-b) Voltage-capacity profiles for the NFM/HC full cell at cycles 10, 100, and 300 (a) and for the NFM-Ca2/HC full cell at cycles 10, 300, 500, 700, and 900 (b), measured at 0.5 V to 3.9 V. (c-e) EIS fitting results for the aged cells: NFM (c), NFM-Ca2 (d), and NFM-Ca4 (e). The total impedance is the sum of R1, R2, R3 and R4 (if relevant).

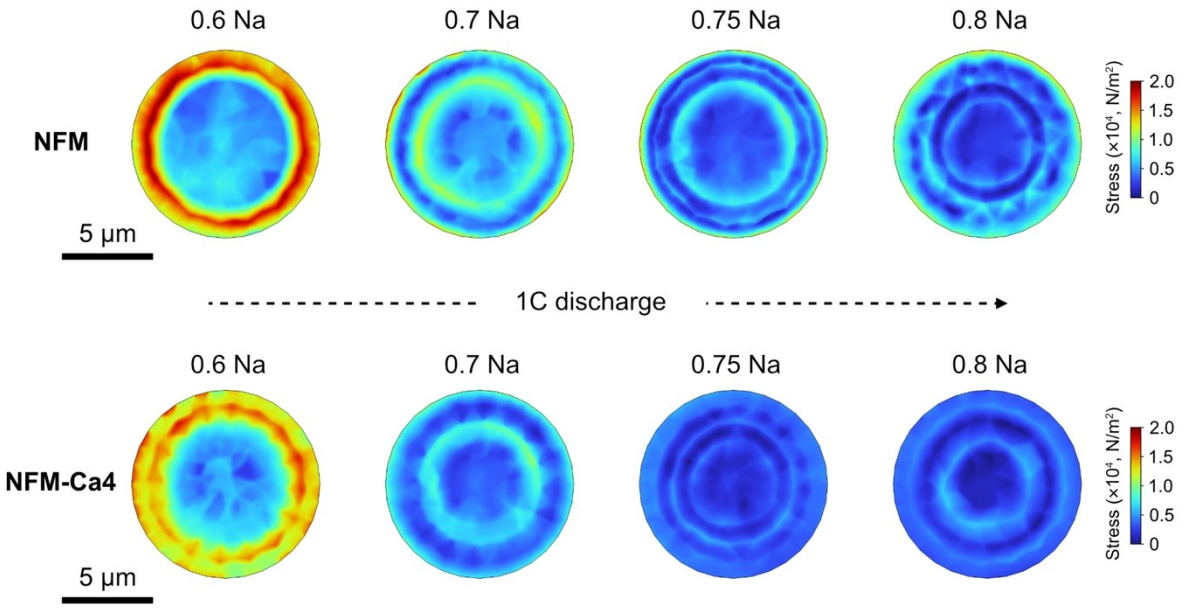

Figure S35. Numerical simulation results for the distribution of von Mises stress in the NFM (top panel) and NFM-Ca4 (bottom panel) during discharge at a rate of 1C.

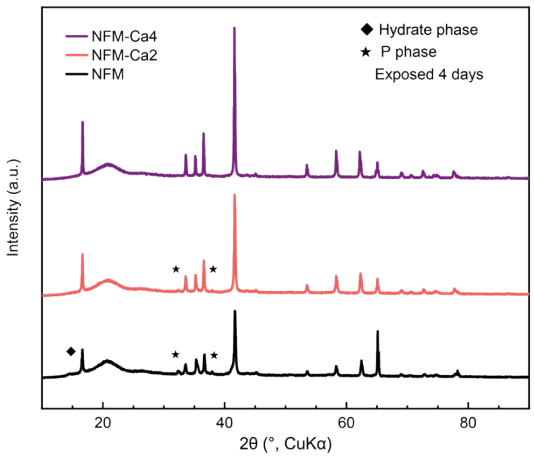

Figure S36. PXRD patterns of NFM, NFM-Ca2 and NFM-Ca4 samples after 4 days of air exposure.

Reference (Supplementary Information)

1. L. Li, G. Tan, J. Tao, Z. Lun and C. Xu, *ACS Appl. Energy Mater.*, 2023, **6**, 6883-6889.
2. J. Filik, A. W. Ashton, P. C. Y. Chang, P. A. Chater, S. J. Day, M. Drakopoulos, M. W. Gerring, M. L. Hart, O. V. Magdysyuk, S. Michalik, A. Smith, C. C. Tang, N. J. Terrill, M. T. Wharmby and H. Wilhelm, *Journal of Applied Crystallography*, 2017, **50**, 959-966.
3. L. Monico, L. Cartechini, F. Rosi, W. De Nolf, M. Cotte, R. Vivani, C. Maurich and C. Miliani, *Scientific Reports*, 2020, **10**, 14337.
4. B. Ravel and M. Newville, *J Synchrotron Radiat*, 2005, **12**, 537-541.
5. L. Wang, T. Maxisch and G. Ceder, *Physical Review B*, 2006, **73**, 195107.
6. A. Jain, G. Hautier, C. J. Moore, S. Ping Ong, C. C. Fischer, T. Mueller, K. A. Persson and G. Ceder, *Computational Materials Science*, 2011, **50**, 2295-2310.
7. Y. Wang, Z. Feng, P. Cui, W. Zhu, Y. Gong, M.-A. Girard, G. Lajoie, J. Trottier, Q. Zhang, L. Gu, Y. Wang, W. Zuo, Y. Yang, J. B. Goodenough and K. Zaghib, *Nat. Commun.*, 2021, **12**, 13.
8. F. Ding, H. Wang, Q. Zhang, L. Zheng, H. Guo, P. Yu, N. Zhang, Q. Guo, F. Xie, R. Dang, X. Rong, Y. Lu, R. Xiao, L. Chen and Y.-S. Hu, *J. Am. Chem. Soc.*, 2023, **145**, 13592-13602.
9. X. Zhu, H. Dong, Y. Liu, Y.-H. Feng, Y. Tang, L. Yu, S.-W. Xu, G.-X. Wei, S. Sun, M. Liu, B. Xiao, R. Xu, Y. Xiao, S. Chou and P.-F. Wang, *ACS Nano*, 2024, **18**, 32003-32015.
10. X.-B. Zhong, C. He, F. Gao, Z.-Q. Tian and J.-F. Li, *Journal of Energy Chemistry*, 2021, **53**, 323-328.
11. A. Rudola, A. J. R. Rennie, R. Heap, S. S. Meysami, A. Lowbridge, F. Mazzali, R. Sayers, C. J. Wright and J. Barker, *Journal of Materials Chemistry A*, 2021, **9**, 8279-8302.